5-22-2019

Building Arc Crust: Plutonic to Volcanic Connections in an Extensional Oceanic Arc, the Southern Alisitos Arc, Baja California

Rebecca A. Morris
Western Washington University

Susan M. DeBari
Western Washington University, debari@wwu.edu

Cathy Busby
University of California, Davis

Sarah Medynski
University of California, Davis

Brian R. Jicha
University of Wisconsin-Madison

Recommended Citation

Morris, R.A., S.M. DeBari, C.J. Busby, S. Medynski, Jicha, B. (2019), Building arc crust – plutonic to volcanic connections in an extensional island arc, the Alisitos arc crustal section, Baja California, Journal of Petrology, v. 60, no.6, p. 1195-1228. https://doi.org/10.1093/petrology/egz029

JOURNAL OF PETROLOGY

Journal of Petrology, 2019, Vol. 60, No. 6, 1195–1228
doi: 10.1093/petrology/egz029
Advance Access Publication Date: 22 May 2019
Original Article

OXFORD

Building Arc Crust: Plutonic to Volcanic Connections in an Extensional Oceanic Arc, the Southern Alisitos Arc, Baja California

Rebecca A. Morris[1]*, Susan M. DeBari[1], Cathy Busby[2], Sarah Medynski[2] and Brian R. Jicha[3]

[1]Geology Department, Western Washington University, Bellingham, WA 98225, USA; [2]Department of Earth and Planetary Sciences, University of California Davis, Davis, CA 95616, USA; [3]Department of Geoscience, University of Wisconsin–Madison, Madison, WI 53706, USA

*Corresponding author. E-mail: ramorri@uvic.ca

Received June 3, 2018; Accepted May 7, 2019

ABSTRACT

The ~50 km long Rosario segment of the Cretaceous Alisitos oceanic arc terrane provides undeformed three-dimensional exposures of the upper 7 km of an oceanic extensional arc, where crustal generation processes are recorded in both the volcanic and underlying plutonic rocks. These exceptional exposures allow for the study of the physical and chemical links between the rock units and help constrain the differentiation processes active during the growth and evolution of arc crust. This study focuses on the southern third of the Rosario segment, previously referred to as the southern volcano-bounded basin, and its plutonic underpinnings. Upper crustal rocks in the Rosario segment consist of a 3–5 km thick volcanic–volcaniclastic section with hypabyssal intrusions. Plutons intrude these units at various levels along-strike, but at each intrusive contact the transition is complete over a distance of <150 m, where stoped volcanic blocks are present. There is striking compositional overlap in whole-rock and mineral chemistry between the plutonic and volcanic units, suggesting a comagmatic source. Whole-rock geochemistry shows coherent trends in major and trace elements in mafic to intermediate compositions, but less coherent trends above 63 wt % SiO_2. Units are predominantly low-K with flat rare earth element patterns, and show large ion lithophile element enrichment and high field strength element depletion. Initial Nd and Pb isotope ratios overlap for all units and imply no cratonic continental involvement. This agrees with low Sr/Y ratios of all rock types, indicative of thin, immature oceanic arc crust. Modeling results show that closed-system fractional crystallization drove crustal differentiation from mafic to intermediate compositions, but open-system processes likely occurred to produce some of the felsic compositions. Differentiation occurred in a two-step fractionation process. Step 1, from basaltic andesite to andesite, fractionated an anhydrous gabbroic cumulate (~40% crystallization). Step 2, from andesite to rhyolite, fractionated a hydrous amphibole cumulate (~65% crystallization, total), which is similar to what fluid dynamical models suggest for production of rhyolite (between 50–70% crystallization). Our results can be used as a reference model for differentiation processes relating to the growth of the middle and upper crust within active extensional arc systems. The Rosario segment plutonic rocks may be analogous to the low-velocity zone ($V_p = 6{\cdot}0$–$6{\cdot}5$ km s^{-1}) imaged within the extensional Izu–Bonin arc. The chemistry of the plutonic and volcanic rocks is most similar to those of volcanic rocks in the Izu–Bonin active rift.

Key words: extensional oceanic arc; plutonic–volcanic connection; closed-system fractional crystallization; arc magmatism; Izu–Bonin analog

INTRODUCTION

Continental crust formation and growth is thought to occur dominantly from island arc accretion and magmatic emplacement at convergent plate margins (Rudnick, 1995). Thus, it is a high research priority to understand how continental crust is generated at island arcs (e.g. DeBari & Sleep, 1991; Garrido *et al.*, 2006; Greene *et al.*, 2006; Jagoutz, 2010; D'Souza *et al.*, 2015; Jagoutz & Kelemen, 2015; Jagoutz & Klein, 2018). Recent intense efforts at studying active oceanic arcs, especially through the International Ocean Discovery Program (IODP), have dovetailed with the National Science Foundation's MARGINS/GeoPRISMS Focus Sites (IODP Science Plan, Bickle *et al.*, 2013; NSF GeoPRISMS Implementation Plan, Morgan *et al.*, 2013). This study presents a unique approach for understanding the generation of juvenile arc crust, by studying an exposed paleo-arc section, the Cretaceous Alisitos oceanic arc in Baja California, Mexico. Exceptional three-dimensional (3-D) paleo-arc exposures in this extensional arc system allow the study of the physical and chemical links between the units that comprise this arc, and constrain the petrological processes active during its growth. These results are used as an analog for processes occurring at depth within active extensional oceanic arcs, such as the Izu–Bonin arc in the western Pacific.

Continental crust is thought to be generated at island arcs through differentiation of high-MgO parental magmas that were themselves derived by complex interactions between fluxes from the mantle wedge and the subducting slab. This differentiation to lower-MgO and higher-SiO_2 magma occurs through fractional crystallization of sub-Moho derived magmas, and is subjected to varying degrees of open-system processes such as assimilation of pre-existing crust or mixing with crustal and/or recharge melts (Haraguchi *et al.*, 2003; Straub, 2008; Jagoutz, 2010; DeBari & Greene, 2011; Garrison *et al.*, 2012). As a result of these complicated processes, magmas erupted in arcs are often very different in composition and mineralogy from the parental magmas that entered the crust at its base. The goal of this study is to understand these magmatic differentiation processes.

There is particular interest in understanding the linkage between volcanic units and the underlying plutonic rocks in arcs, both physically and chemically, and constraining magma production rates (e.g. Jicha & Jagoutz, 2015; Lipman & Bachmann, 2015). Deciding whether volcanic deposits are geochemically linked to their associated plutonic rocks helps to constrain differentiation processes within these systems. Additionally, geochemical fingerprinting can be used to determine whether the volcanic and plutonic units are derived from one or multiple mantle-derived components. This study uses geochemical data from the volcanic deposits and plutonic rocks to determine how this crust was generated and how it evolved.

The Cretaceous Alisitos oceanic arc (Fig. 1a) provides a remarkable opportunity to explore the evolution of crust during its entire growth history. Exposed paleo-arc sections often display the heterogeneity that exists within the upper crust, along with vertically stratified crustal exposures that may form through differentiation processes (DeBari & Greene, 2011). The Rosario segment of the Alisitos arc (Fig. 1b) provides exposures of a heterogeneous upper volcanic crust that shows a transition downwards into underlying plutonic rocks. This segment has previously been described as one of the largest and best-exposed intact sections of the upper to middle crust of an oceanic arc terrane (Busby *et al.*, 2006). The segment is therefore an exceptional location to study juvenile arc growth, not only because of its relative ease of accessibility, but also because it is structurally intact and minimally altered (ranging from unaltered to non-pervasive, lower greenschist facies; Busby *et al.*, 2006).

The Alisitos has been proposed to be an excellent field analog to the active Izu–Bonin arc. They are both intra-oceanic extensional arcs (e.g. Stern *et al.*, 2003; Busby *et al.*, 2006), which are ideal locations to study generation processes of juvenile continental crust. Seismic studies in the Izu–Bonin arc have shown a distinct low-velocity ($V_p = 6{\cdot}0$–$6{\cdot}5\,km\,s^{-1}$) middle crust (Suyehiro *et al.*, 1996); however, establishing the lithological equivalents to this velocity is challenging. Exceptional field exposures of the Alisitos arc allow for a larger contextual study than the limited information that may be provided by a one-dimensional (1-D) drill core from the Izu–Bonin arc (Busby *et al.*, 2006; DeBari *et al.*, 2013). One aim of this study is to understand the plutonic to volcanic connection (e.g. Bachmann & Huber, 2016; Lundstrom & Glazner, 2016) recorded within the middle to upper arc crust, as this transition is very well exposed within the Rosario segment of the Alisitos arc.

Within the larger goal of understanding petrological processes of juvenile island arc construction, our specific research outcomes are (1) a description of the physical and geochemical relationships between plutonic and volcanic rocks, (2) tests of hypotheses for magma differentiation within the plutonic and volcanic rocks, and (3) presentation of a crustal evolution model. The data presented are from a subset of the Alisitos arc, the southern third of the Rosario segment, characterized by Busby *et al.* (2006) as the southern volcano-bounded basin with plutonic underpinnings (Fig. 1b). The southern region has the best exposures and greatest range of compositions for the hypabyssal and plutonic rocks, which is why it was chosen for the most detailed mapping, densest geochemical sampling, and application of the broadest range of analytical techniques. Additional petrogenetic data from the rest of the Rosario segment (Medynski *et al.*, 2016) are consistent with the data provided here, indicating that our geochemical results and the modeling presented are applicable to the entire Rosario segment. We show here that overall, fractional

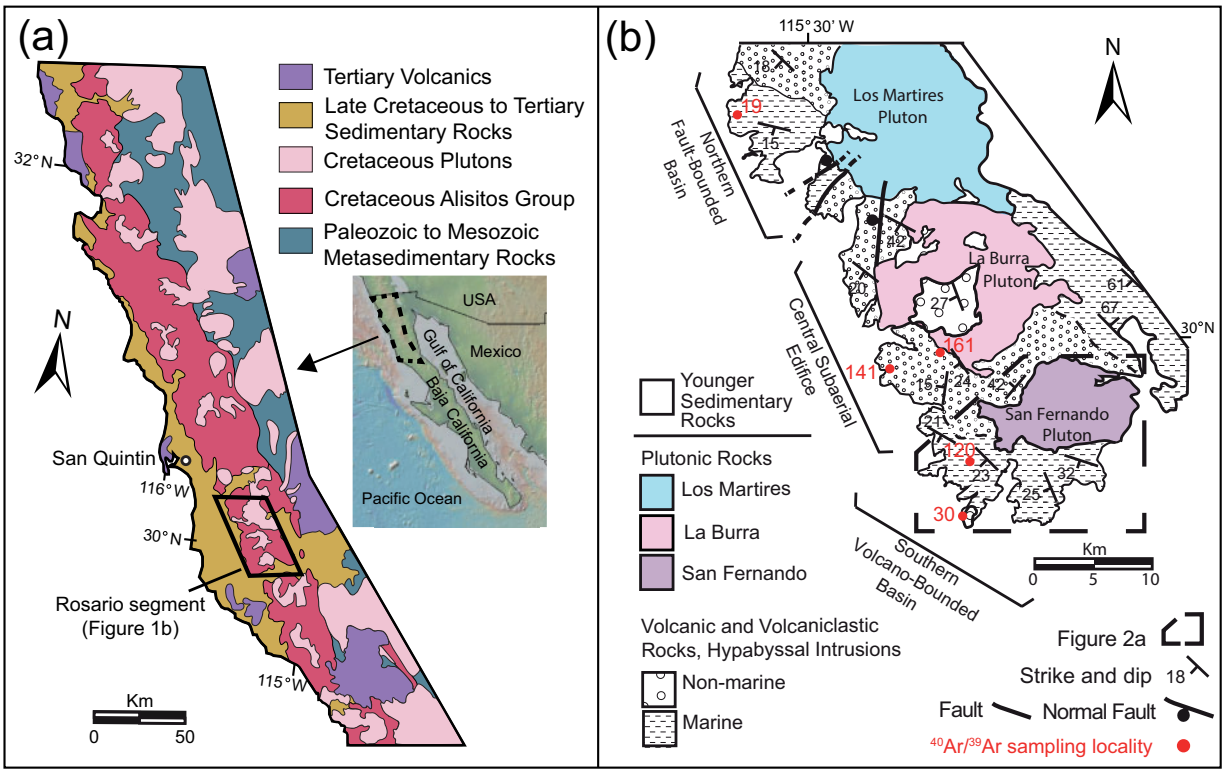

Fig. 1. (a) Simplified geological map from Busby *et al.* (2006) of the Cretaceous Alisitos oceanic arc, Baja California, Mexico, showing the Rosario segment outlined in black. (b) Simplified geological map of the Rosario segment modified from Fackler-Adams & Busby (1998). The segment includes a northern fault-bounded basin, a central subaerial edifice, and a southern volcano-bounded basin (Busby *et al.*, 2006). Plutonic units intrude the 3–5 km thick volcanic–volcaniclastic upper crustal section, which dips west. Sample locations for $^{40}Ar/^{39}Ar$ ages are shown in red. This paper focuses mainly on the southern volcano-bounded basin (dashed-line outline), shown in Fig. 2a.

crystallization was likely the main driver of differentiation from mafic to intermediate compositions, and open-system processes likely occurred to some degree to produce some of the more felsic compositions.

GEOLOGICAL SETTING

The Alisitos arc is a 600 km long × 50 km wide accreted oceanic arc terrane (Fig. 1a; Gastil *et al.*, 1975; Busby *et al.*, 1998; Busby, 2004). It formed during the Early Cretaceous in response to intra-oceanic subduction marginal to Mexico (Busby, 2004; Busby *et al.*, 2006). This was followed by mid-Cretaceous back-arc basin closure and underthrusting of the arc beneath Paleozoic to Mesozoic Mexican continental margin rocks (Busby *et al.*, 1998; Busby, 2004). A Late Cretaceous continental margin batholith (~98–90 Ma) stitched this suture ~20 km east of the study area (Fig. 1a; Busby, 2004).

The Rosario segment is located in the southern part of the Alisitos arc (Fig. 1a), where desert exposures are excellent and the rocks are undeformed (Busby *et al.*, 2006). The Rosario segment forms a 50 km long × 30 km wide monoclinal section that dips westward 10–30°, passing upward (westward) from plutonic rocks to volcanic–volcaniclastic rocks and hypabyssal intrusions (Fig. 1b; Busby *et al.*, 2006). It has syn-depositional normal faults, but no post-depositional faults (Busby, 2004; Busby *et al.*, 2006). These syn-depositional faults, along with the presence of silicic calderas and high tectonic subsidence rates, led Busby and others to the interpretation that the Alisitos arc formed under an extensional tectonic regime (Busby-Spera & Boles, 1986; Fackler-Adams & Busby, 1998; Busby, 2004).

The Rosario segment is divided into three subsegments (Fig. 1b), from north to south: a northern fault-bounded basin, a central subaerial edifice, and a southern volcano-bounded basin (Busby *et al.*, 2006). Each of these segments is underlain by plutons that intrude upward through the volcanic wall rocks between them. These plutons are (from north to south) the Los Martires, La Burra, and San Fernando (Fig. 1b; Busby *et al.*, 2006). The volcanic section is up to 5 km thick, and is unconformably overlain (to the west) by Late Cretaceous to Tertiary sedimentary rocks (Fig. 1b; Fackler-Adams & Busby, 1998; Busby, 2004; Busby *et al.*, 2006). The entire volcanic and plutonic crustal section of the Rosario segment was previously inferred to have formed in about 1·5 Myr, based on U–Pb zircon ages (Busby *et al.*, 2006), but our new age data suggest that it may have taken longer (about 8 Myr).

Previous work focused on field descriptions of the Rosario segment, with limited details on the relationships between the plutonic and volcanic units, limited petrographic descriptions, and no geochemical data (Fackler-Adams, 1997; Busby *et al.*, 2006). The geological map of the Rosario segment of the Alisitos arc has been updated, based on new field observations combined with new geochemical and petrographic data (Medynski *et al.*, 2016; and this study, Fig. 2).

MAP UNITS AND FIELD RELATIONS

The southern volcano-bounded basin includes the following principal types of map units, divided by composition into mafic, intermediate, and felsic (for plutonic rocks) or silicic (for volcanic rocks) (Fig. 2): (1) plutonic rocks; (2) hypabyssal intrusions; (3) strata, further divided into lavas, lava domes, block-and-ash-flow tuffs, ignimbrites, volcaniclastic rocks, and biogenic rocks; and (4) unclassified volcanic rocks (outcrop characteristics and field relationships preclude distinction as a lava or hypabyssal intrusion). Petrographic descriptions are summarized in Table 1.

The San Fernando pluton underpins the southern volcano-bounded basin (Fig. 1b), and the stratified units dip fairly uniformly westward, so depths within intrusive parts of the section are taken to be perpendicular to the dip of the strata (Fig. 3). The southern volcano-bounded basin is unconformably overlain by Late Cretaceous sedimentary rocks. The following descriptions focus on the field characteristics of the map units.

Plutonic rocks

The contact between the San Fernando pluton and the overlying volcanic units is intrusive, and the transition between them (i.e. entirely plutonic to entirely volcanic) occurs over a paleo-vertical distance of ~150 m. In this transition, volcanic megablocks are surrounded by plutonic rocks, indicative of stoping. The main body of the pluton has a felsic to intermediate tonalitic interior (Kpsf-f/i, Fig. 2) with localized regions of hornblende gabbro at the margins and lesser volumes in the interior (Kpsf-m, Fig. 2). Magma mingling relations are well-exposed along the margins, and indicate that the felsic to intermediate tonalite and gabbro are coeval (Fig. 4a). Mixed hybrid tonalite comprises complex mixtures of gabbro and tonalite. Two-pyroxene gabbros (Kpsf-ma, Fig. 2) are present in the eastern interior and deepest part of the pluton, but are rarely interspersed (<1% of the plutonic unit). Hornblende-bearing enclaves are abundant throughout the felsic to intermediate tonalitic interior and generally range from 5 to 20 cm in size. Their shapes are commonly bulbous equant blebs, and, in some cases, are slightly flattened or lobate (Fig. 4b). Hornblende cumulates occur within the hornblende gabbro, and rare felsic plagioclase cumulates occur within the main tonalitic body.

Felsic intrusions that cross-cut the main phase tonalite body are coarse-grained and range from centimeter-scale (<0·5 m) to meter-scale (~5 m). These intrusions are leucocratic (primarily plagioclase + quartz ± K-feldspar ± hornblende ± trace titanite), and intrude the hornblende gabbro margin and overlying volcanic rocks. They range in width from <10 cm – 5 m, and can be followed for up to 25 m within the overlying volcanic rocks. Both brittle and ductile characteristics are displayed between the felsic intrusions and gabbroic margin, where sharp contacts and well-mixed zones are evident. Where these felsic intrusions extend into the overlying volcanic rocks, they commonly include angular xenoliths of fine-grained country rock, ranging from centimeter-scale (<0·5 m) to meter-scale (<5 m) (Fig. 4c). These felsic intrusions may have resulted from the extraction of silicic interstitial melt from nearby tonalite mush (e.g. Bachmann & Bergantz, 2004).

We calculated a volume estimate for the San Fernando pluton based on exposure extent and the regional dip of the arc crustal section. Using an areal extent of 120 km^2, and observed thickness of 2·5 km, this estimate ranges from approximately 150 km^3 to 400 km^3, with the latter volume more likely because we assume that pluton thickness extends towards the SW to directly underlie the volcanic edifice (i.e. San Fernando ignimbrite and nearby shallow intrusions) (Fig. 3).

Hypabyssal intrusions

Hypabyssal intrusions (Kh, Fig. 2) occur throughout the volcanic section and are distinguished by their discordant (dikes and plugs) or concordant (sills) relation to stratified units, as well as a lack of flow breccias common in the lavas. Dikes have chilled margins and coarser interiors and are <5 m wide (Fig. 4d). They are locally altered, with epidote along their margins. Sills form as sheets or lenses within stratified units, have chilled margins, and may occur as multiple stacked sills up to 80 m thick. Some sills show complex, lobate pillow-like contacts with the surrounding volcaniclastic host, indicative of mixing with an unconsolidated, water-saturated host (i.e. a peperite). These peperites are similar to those described elsewhere in the Alisitos arc (Busby-Spera & White, 1987; White & Busby-Spera, 1987). Plugs are more irregularly shaped than sills or dikes, commonly forming pod-shaped intrusions, and may pass laterally or up- or down-section into broad irregularly shaped sill-like and dike-like intrusions. Hypabyssal intrusions may have flow banding, spherulites, and columnar jointing (Fig. 4e). Xenoliths occur within some hypabyssal intrusions, and range from centimeter-scale to meter-scale (Fig. 4f).

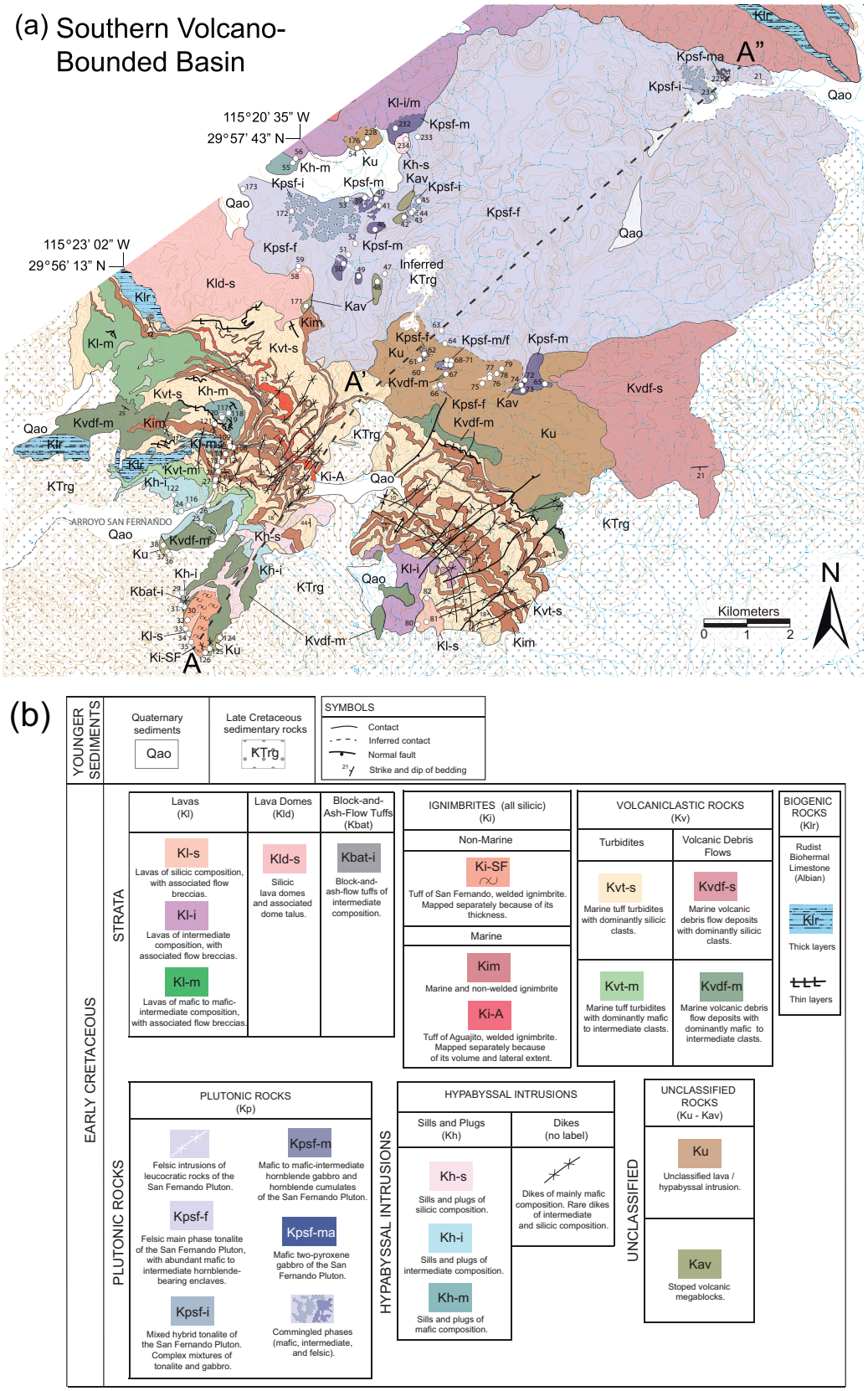

Fig. 2. (a) Geological map of the southern volcano-bounded basin of the Rosario segment (Alisitos arc). Map units include: (1) plutonic rocks; (2) hypabyssal intrusions; (3) strata, including lavas, lava domes, block-and-ash-flow tuffs, ignimbrites, volcaniclastic rocks, biogenic rocks, and younger sedimentary rocks; and (4) unclassified volcanic rocks (outcrop characteristics and field relationships preclude distinction as a lava or hypabyssal intrusion). Sample locations are indicated on the map (white circles). The cross-section corresponding to A–A'–A" is presented in Fig 3. (b) Map key for lithological units shown in (a) and Fig. 3.

Table 1: Petrographic summary

Lithologic unit and lithofacies	Phenocryst %	Phenocryst/ mineral modes	[1]Mg# or An#	[2]Mineral shapes	Notes
Stratified rocks					
Ignimbrites	<6% fragments <15% lithics	Plag (85–90%) Hbld (<10%)		broken crystals	Lithic-free to lithic-rich (monomict) ignimbrites. Pumices are slightly welded to welded.
Lavas, and block-and-ash-flow tuffs	<5–35%	Plag (50–90%) Hbld (0–30%) Cpx (0–20%) Oxides (<10%)	45–58 65–70 	eu–sub sub–an eu–an sub–an	Lavas are generally phyric, with glomerocrysts of plag + cpx +/- hbld. Some silicic lavas have cm-scale (<5 cm) xenoliths with a fine-grained hbld + plag groundmass. Sampled blocks are phyric with plag + hbld + oxides.
Hypabyssal intrusions					
Dikes and sills	0–40%	Plag (50–100%) Hbld (0–35%) Cpx (5–50%) Opx (0–5%) Oxides (<15%) Qtz (<10%)	 59–82 58–65 	eu–sub sub–an eu-an eu–sub eu–an an	Dikes are generally phyric, with glomerocrysts of plag + cpx +/- opx (mafic and intermediate dikes) or plag + hbld (silicic dikes). Some dikes display coarser groundmass compared to sills. Sills are generally aphyric to slightly phyric. Slightly phyric sills commonly display flow banding or devitrified groundmass textures, and have felsic xenoliths. Rare sills display hypidiomorphic granular texture.
Plutonic rocks					
Hornblende gabbro[3]		Plag (40–80%) Hbld (15–55%) Oxides (<10%)	63–92 57–68 	eu–sub sub–an an	Hypidiomorphic granular texture. Primary hornblende is classified as magnesio-hbld or magnesio-ferri-hbld. Hbld-bearing enclaves have similar modal percentages and textures, but are finer-grained.
Two-pyroxene gabbro		Plag (60–65%) Opx (10–15%) Cpx (5–10%) Hbld (<5%) Bt (<5%) Oxides (<10%)	54–88 67–68 76 70–71 61–63 	eu–sub eu–sub sub–an an an eu–sub	Hypidiomorphic inequigranular texture. Pyroxenes display sieved textures. Magnesio-ferri-hbld occurs interstitially.
Tonalite[4]		Plag (40–60%) Qtz (20–50%) Hbld (5–25%) Bt (<10%) K-spar (<5%) Oxides (<5%) Titanite (<1%)	43–52 	eu–sub an an an an sub–an an	Hypidiomorphic granular texture. Bt is uncommon, and where present generally occurs as rims around hbld grains. Titanite is common, but occurs in very minor (≪1%) amounts.
Mixed hybrid tonalite		Plag (40–60%) Qtz (30–50%) Cpx (10–15%) Hbld (<5%) Oxides (<5%) Titanite (<1%)	 82–85 79–80 	eu–sub an sub–an an sub–an an	Hypidiomorphic inequigranular texture. Cpx displays sieved textures. Magnesio-ferri-hbld occurs interstitially. Titanite is common, but occurs in minor (<1%) amounts.
Leucocratic rocks		Plag (15–40%) Qtz (40–70%) K-spar (<30%) Hbld (<10%) Oxides (<1%) Titanite (<1%)	 	eu–sub sub–an sub–an an sub–an an	Hypydiomorphic inequigranular texture. Some qtz grains display micrographic intergrowth textures with feldspar. Titanite is common, but occurs in minor (<1%) amounts.

[1]Mg# and An# from core compositions. [2]Abbreviated mineral shapes correspond to euhedral (eu), subhedral (sub), and anhedral (an). [3]Hornblende gabbro unit includes hornblende cumulates and hornblende-bearing enclaves. [4]Tonalite unit includes felsic plagioclase cumulates. Cumulates were defined based on mineral modal percentages and whole-rock trace element chemistry (Table 2).

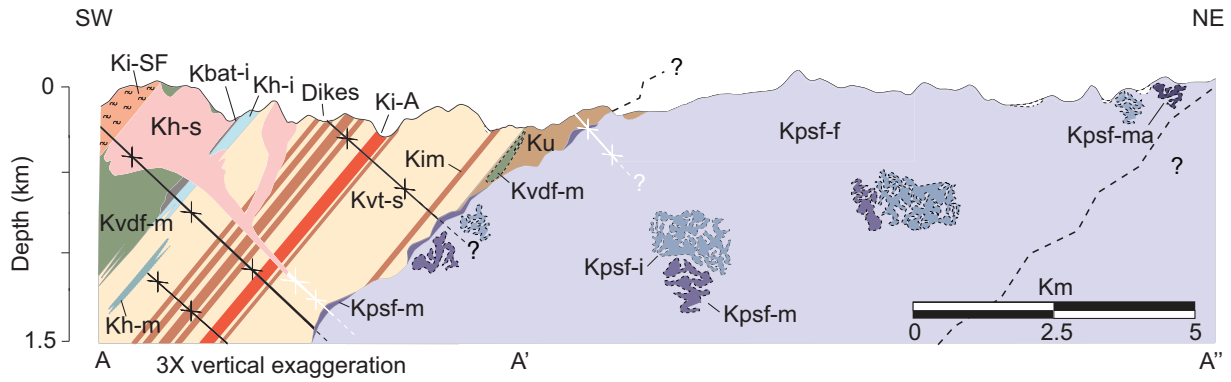

Fig. 3. Cross-section line A–A′–A" (from Fig. 2a), representing the field relationships established between the intrusive plutonic source rocks and overlying volcanic units within the southern volcano-bounded basin (see Fig. 2b map key). 3X vertical exaggeration is used to display the stratigraphic units.

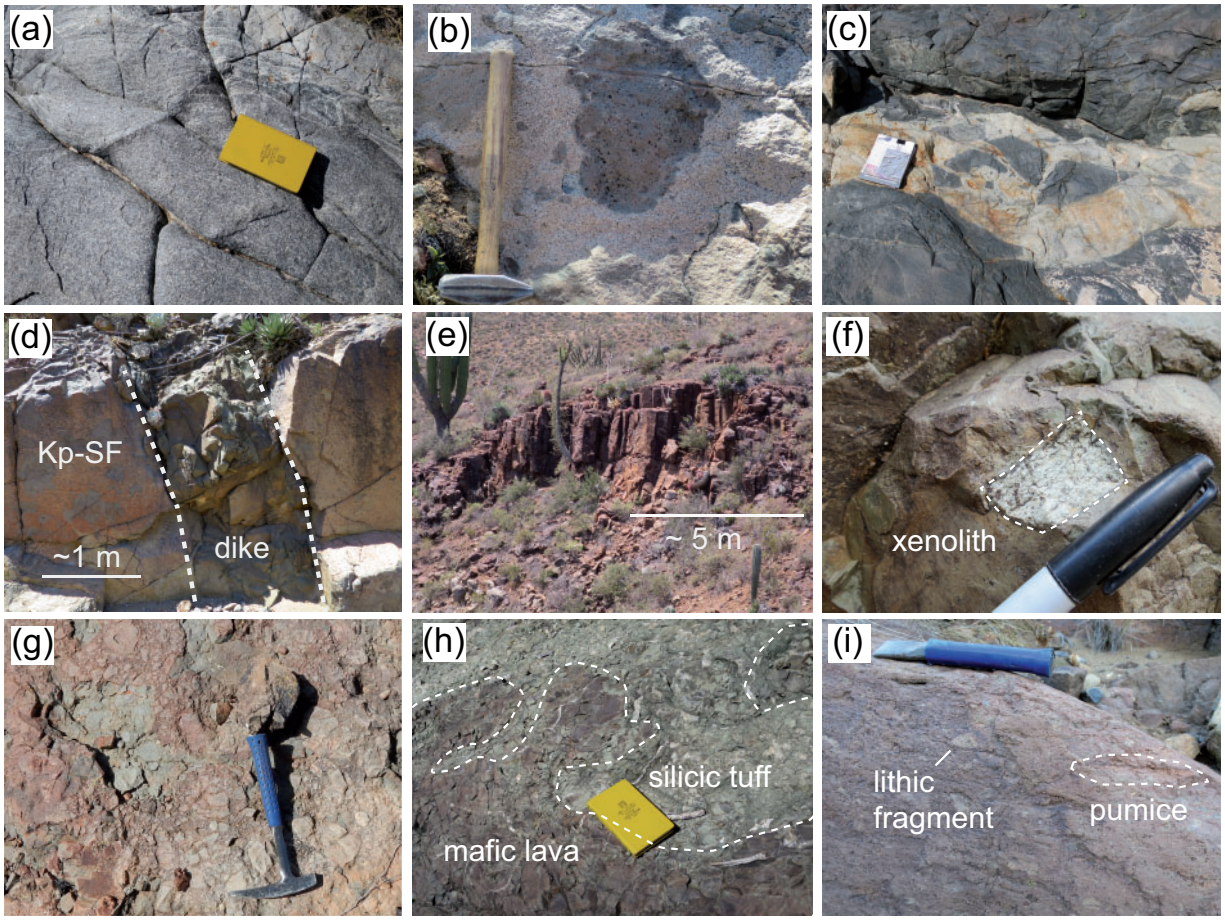

Fig. 4. Field photographs. (a) Magma mingling features preserved in the San Fernando pluton near the contact with the overlying volcanic rocks. Light areas in the top right represent felsic compositions; darker areas in the bottom left represent mafic compositions. (b) Hornblende-bearing enclaves within the tonalitic interior of the pluton, note the miarolitic cavities in the enclaves. (c) Xenoliths of fine-grained volcanic country rock within felsic intrusions of leucocratic rocks that extend into the overlying volcanic rocks. (d) Dikes display vertical to subvertical cross-cutting relationships with stratified units (e.g. tuff of San Fernando is cross-cut in the photograph). (e) Sills are concordant with the surrounding stratified units and commonly display flow banding, spherulites, and columnar jointing (shown). (f) Felsic xenoliths occur within some sills and dikes, and can reach diameters of up to 1·5 m. (g) Lavas display bottom flow breccia. (h) Peperitic margins identified where coherent mafic lava intrudes silicic marine tuff turbidites. (i) Non-marine ignimbrites are welded and tens to hundreds of meters thick, with indistinct stratification in the form of alternating pumice-rich (shown) and pumice-poor layers.

Stratified rocks

Lavas, lava domes, and block-and-ash-flow tuffs

Lavas (Kl, Fig. 2) are distinguished from sills by the presence of interstratified flow breccia (Fig. 4g). Flow breccia consists of angular, tightly packed volcanic blocks of uniform composition. Some lavas injected unconsolidated marine tuff turbidites during transport and deposition, producing peperitic margins (Fig. 4h). Block-and-ash-flow tuffs (Kbat, Fig. 2) are very poorly sorted, nonstratified deposits of angular monolithological volcanic blocks and lapilli in an ash matrix; these are interpreted to represent the collapse of lava fronts or lava domes. Lava domes (Kld) are hypabyssal intrusions that pass upward into breccias.

Ignimbrites

Ignimbrites (Ki, Fig. 2) consist of deposits of pumice and ash, tens of meters thick, and are all silicic. They were previously classified by Fackler-Adams (1997) and Busby *et al.* (2006) as either non-marine or marine. Non-marine ignimbrites (Ki-SF) are largely welded and massive, while marine ignimbrites (Kim, Ki-A) are non-welded and crudely stratified with basal load structures where they rest on volcaniclastic sedimentary rocks (Fig. 2). Most ignimbrites are not named separately, but two in the southern volcano-bounded basin are distinctive and extensive enough to be named (Figs 2 and 3): (1) the tuff of Aguajito (Ki-A), which forms a stratigraphic marker across the entire Rosario segment and formed during caldera collapse of the central subaerial edifice (Busby *et al.*, 2006); (2) the tuff of San Fernando (Ki-SF), a non-marine welded ignimbrite at the top of the section. The tuff of San Fernando has a lower and upper cooling unit, totaling 350 m in thickness, separated by a 50 m thick silicic lava. The lower cooling unit is more welded and lithic poor, with a 2–3 m thick basal vitrophyre, and is gray in color, whereas the upper unit is oxidized (red) and is lithic rich (Fig. 4i).

Volcaniclastic rocks

Volcanic debris flow deposits (Kvdf) are massive to crudely stratified beds with angular, coarse-grained, polylithic volcanic clasts, supported in a pebbly sandstone matrix, and occur in both non-marine and marine environments (Fig. 2). Marine tuff turbidites (Kvt) are thin- to very thick-bedded lapilli tuffs and tuffs that are commonly normally graded, and massive or laminated (Fig. 2).

ANALYTICAL METHODS

The following sections describe the analytical methods used for sample collection, whole-rock chemistry (including isotopes), and mineral chemistry (including trace element analyses of amphibole). These analyses provide the foundational data for interpreting magmatic processes in the arc.

Sample collection and field methods

Lithological units described above were sampled to ensure a full representation of the southern volcano-bounded basin. Samples were generally collected in east–west transects to characterize lithological variations from base to top of the section. Variations between lithological units are summarized in Table 1. Although all units have samples with some degree of greenschist-facies hydrothermal overprint (± epidote, chlorite, actinolite), the least-altered samples were chosen for geochemistry. Loss on ignition (LOI), a good indicator of the degree of alteration (Table 2), was determined based on the methods of Lechler & Desilets (1987). Loss on ignition does not correlate with mobile elements such as Rb, Cs, Ba, Sr, and K, but does correlate with Sr-isotope ratios (discussed below).

Whole-rock chemistry

Major and trace element compositions of 55 whole-rock samples were obtained via X-ray fluorescence spectrometry (XRF) and inductively coupled plasma mass spectrometry (ICP-MS) at the Washington State University (WSU) GeoAnalytical Laboratory (Table 2). Sample preparation for major and trace element chemistry was conducted at both Western Washington University (WWU) and WSU. Lithium tetraborate fused glass beads were prepared by powdering fresh rock chips following the methods of Knaack *et al.* (1994), Johnson *et al.* (1999), and Steenberg *et al.* (2017). Sample preparation and processing of glass beads are described in Supplementary Data Electronic Appendix 1; supplementary data are available for downloading at http://www.petrology.oxfordjournals.org.

Analysis by XRF measured 10 major element oxides (SiO_2, TiO_2, Al_2O_3, FeO_{total}, MnO, MgO, CaO, Na_2O, K_2O, and P_2O_5) and 13 trace elements (Sc, V, Ni, Cr, Ba, Sr, Zr, Y, Rb, Nb, Ga, Cu, and Zn). Analysis by ICP-MS provided results for 14 rare earth elements (REE), as well as Ba, Th, Nb, Y, Hf, Ta, U, Pb, Rb, Cs, Sr, Sc, and Zr. Data accuracy was estimated by the GeoAnalytical Laboratory at WSU by analyzing repeat samples and certified reference materials (GeoPT certification samples for XRF, consensus GeoReM values for ICP-MS) that were run within the sample stream. Maximum measured differences (in wt %) for accuracy between known values and WSU results for XRF-analyzed major elements are: $<0{\cdot}2\%$ for SiO_2 and FeO_{total}; $<0{\cdot}07\%$ for MgO, Al_2O_3, CaO, Na_2O, and K_2O; and $<0{\cdot}01\%$ for TiO_2, MnO, and P_2O_5. Trace elements analyzed and reported by XRF include Zr and Rb (see Supplementary Data Electronic Appendix 1), which are accurate to 3·0 and 1·1 ppm, respectively. Certified reference materials and GeoPT certification samples used to determine analytical accuracy (i.e. slopes of measured concentration versus certified concentration) produced linear regressions of $>0{\cdot}99$ for all reported XRF analyses (major elements, Zr, and Rb). Maximum measured differences (in ppm) for accuracy between known values and WSU results

Table 2: Whole-rock major element (wt %) and trace element (ppm) composition

	Ignimbrites			Lavas, block-and-ash-flow tuffs						Hypabyssal intrusions	
Sample:	32	35A	35B	33A	33B	34	80	30	106	31	121
Latitude (°N):	29·86697°	29·86176°	29·86176°	29·86526°	29·86526°	29·86333°	29·86504°	29·86947°	29·90098°	29·86937°	29·90373°
Longitude (°W):	115·37061°	115·36987°	115·36987°	115·37141°	115·37141°	115·37007°	115·31807°	115·37161°	115·36028°	115·37154°	115·36323°
SiO_2	69·34	70·96	68·23	65·27	65·42	68·77	70·56	59·19	54·64	66·19	65·74
TiO_2	0·67	0·68	0·70	0·92	0·91	0·74	0·42	1·02	1·70	0·83	0·96
Al_2O_3	13·34	13·59	14·95	15·07	14·84	14·14	14·80	16·52	14·75	14·73	14·36
FeO*	5·34	5·00	5·05	6·63	6·54	5·40	4·23	8·22	12·34	7·62	7·01
MnO	0·17	0·11	0·18	0·24	0·23	0·16	0·11	0·22	0·31	0·27	0·12
MgO	0·93	0·91	1·48	2·01	2·22	1·43	0·98	2·13	4·04	2·63	2·05
CaO	4·57	2·35	2·98	4·41	4·19	3·73	0·69	9·10	7·98	3·29	3·68
Na_2O	4·55	5·21	5·50	4·88	4·34	4·55	6·17	3·06	3·16	3·26	4·59
K_2O	0·94	1·04	0·76	0·36	1·09	0·88	1·90	0·42	0·84	1·00	1·28
P_2O_5	0·15	0·14	0·18	0·21	0·21	0·18	0·15	0·13	0·23	0·18	0·22
LOI	4·62	1·88	2·17	3·45	1·42	1·25	1·97	4·43	2·17	3·65	2·87
Mg#	23·7	24·4	34·4	35·0	37·7	32·1	29·2	31·6	36·9	38·0	34·2
Rb	14·1	10·4	4·8	4·0	6·1	13·3	26·3	5·8	17·1	14·5	23·9
Sr	124	200	209	282	139	215	131	198	250	168	163
Zr	80	113	148	100	70	109	134	97	104	108	174
Ba	258	379	252	201	247	325	1757	166	207	284	194
Sc	20·9	20·6	21·6	26·4	18·4	22·2	8·9	30·9	41·3	22·8	22·8
V	35	34	23	87	83	46	44	229	364	105	55
Cr	4·3	3·8	1·2	6·1	5·6	4·9	1·5	16·6	<d·l	6·6	1·8
Ni	2·57	2·38	2·18	3·27	4·65	3·76	2·94	11·09	14·68	5·05	0·88
Cu	14·0	55·9	64·1	18·8	10·7	23·4	1·5	10·3	150·8	5·9	6·6
Zn	84·3	103·6	181·0	143·4	146·4	120·0	69·7	106·1	58·5	169·0	49·7
Ga	15·2	15·4	16·8	16·3	17·7	17·2	15·5	17·4	17·3	16·4	15·4
Y	37·8	43·1	56·3	38·5	26·1	42·8	35·0	32·7	46·0	36·4	51·8
Nb	2·23	2·81	3·35	2·41	1·65	2·62	2·72	1·99	2·48	2·56	3·70
Ta	0·16	0·20	0·24	0·17	0·11	0·18	0·24	0·14	0·20	0·17	0·31
Cs	0·38	0·19	0·13	1·36	0·20	0·43	0·16	0·82	0·53	0·52	0·14
La	7·28	8·09	9·03	7·02	4·84	7·95	13·00	6·01	6·74	5·64	10·01
Ce	17·9	19·7	24·1	17·7	12·3	19·3	24·5	15·1	17·7	15·6	26·2
Pr	2·87	3·24	3·87	2·80	1·96	3·01	3·77	2·36	2·89	2·60	4·12
Nd	14·7	16·4	19·7	14·3	9·7	15·5	17·0	11·7	15·3	13·3	20·2
Sm	4·69	5·28	6·59	4·72	3·28	5·18	4·56	3·87	5·19	4·47	6·40
Eu	1·46	1·55	1·77	1·51	1·04	1·54	1·21	1·17	1·67	1·30	1·62
Gd	5·92	6·66	8·46	5·92	4·12	6·49	5·38	4·90	6·97	5·56	7·83
Tb	1·10	1·23	1·55	1·10	0·75	1·21	0·90	0·92	1·26	1·07	1·44
Dy	7·01	8·09	10·21	7·14	4·84	7·83	5·74	6·02	8·49	7·08	9·32
Ho	1·48	1·72	2·21	1·50	1·05	1·67	1·23	1·28	1·83	1·49	2·01
Er	4·20	4·76	6·09	4·18	2·91	4·60	3·40	3·61	5·16	4·12	5·58
Tm	0·62	0·71	0·92	0·63	0·43	0·70	0·52	0·54	0·75	0·63	0·83
Yb	3·82	4·43	5·56	3·91	2·65	4·34	3·43	3·41	4·69	3·91	5·24
Lu	0·61	0·68	0·85	0·62	0·42	0·68	0·56	0·56	0·72	0·60	0·84
Hf	2·53	3·58	4·63	3·17	2·24	3·44	3·90	2·98	3·31	3·43	5·14
Pb	3·29	5·17	6·93	7·43	3·91	10·26	0·61	5·60	0·81	1·34	0·93
Th	0·82	0·98	1·25	1·01	0·70	0·92	1·72	1·52	0·88	1·00	2·11
U	0·28	0·45	0·53	0·42	0·30	0·38	0·71	0·59	0·37	0·43	0·87

(continued)

Table 2: Continued

	Hypabyssal intrusions										
Sample:	24	25	29	125B	108	28A	28B	28C	28D	70C	118
Latitude (°N):	29·88783°	29·88597°	29·87116°	29·86043°	29·90100°	29·89603°	29·89603°	29·89603°	29·89603°	29·91721°	29·90709°
Longitude (°W):	115·37157°	115·36740°	115·37124°	115·36555°	115·35908°	115·36308°	115·36308°	115·36308°	115·36308°	115·30987°	115·36107°
SiO_2	62·77	62·24	59·87	55·67	55·82	54·98	54·22	54·73	61·24	59·72	55·65
TiO_2	1·42	1·23	0·88	1·09	1·40	1·22	1·39	1·38	1·14	1·14	1·68
Al_2O_3	13·83	13·94	16·74	15·62	15·80	18·13	16·94	15·95	15·07	15·74	14·53
FeO*	9·22	8·92	7·74	10·86	12·20	10·12	10·88	11·38	9·51	8·67	12·50
MnO	0·17	0·17	0·19	0·23	0·30	0·31	0·23	0·24	0·14	0·22	0·20
MgO	2·32	2·45	3·32	4·79	3·92	3·98	2·95	4·22	2·46	2·80	3·73
CaO	4·91	5·27	7·11	7·91	4·61	3·90	8·04	6·89	3·57	6·72	7·92
Na_2O	3·92	3·67	3·44	3·09	5·16	6·37	4·61	4·73	6·57	4·28	3·13
K_2O	1·17	1·92	0·57	0·64	0·60	0·85	0·57	0·30	0·09	0·51	0·43
P_2O_5	0·27	0·19	0·15	0·12	0·20	0·15	0·17	0·17	0·21	0·20	0·23
LOI	1·53	1·48	1·35	4·58	2·78	3·42	5·80	6·19	3·45	0·69	1·40
Mg#	31·0	32·9	43·4	44·0	36·4	41·2	32·6	39·8	31·6	36·5	34·7
Rb	29·4	38·1	7·7	7·0	11·9	18·8	15·5	8·0	1·2	10·7	9·6
Sr	228	210	225	321	255	379	311	331	181	202	202
Zr	190	189	97	57	88	69	77	76	107	103	104
Ba	300	518	228	254	169	631	247	141	43	245	174
Sc	30·0	28·1	26·7	35·8	41·0	37·2	39·2	41·9	28·0	31·1	41·7
V	176	218	177	323	255	290	311	316	162	193	364
Cr	<d·l	4·3	20·7	35·5	1·9	14·3	5·5	29·5	<d·l	7·9	<d·l
Ni	3·76	5·64	14·36	21·47	2·66	11·09	8·91	14·26	3·47	4·43	15·46
Cu	41·7	42·9	54·4	99·4	68·9	67·7	82·1	159·4	5·0	29·7	232·9
Zn	84·8	111·0	120·4	234·8	51·1	109·8	104·2	118·0	72·7	119·5	118·5
Ga	15·4	14·5	17·3	16·0	17·9	18·0	19·0	18·7	18·6	16·4	17·3
Y	54·3	45·4	31·2	22·2	40·5	30·0	33·4	32·5	39·8	28·4	45·8
Nb	4·08	3·69	1·94	1·19	2·14	1·65	1·82	1·84	2·47	2·01	2·44
Ta	0·30	0·26	0·14	0·10	0·19	0·11	0·12	0·12	0·16	0·18	0·21
Cs	0·31	0·23	0·28	0·84	0·53	0·25	1·07	1·35	0·18	0·48	0·21
La	11·11	9·37	6·52	3·41	6·06	5·02	5·12	5·38	6·81	5·34	7·04
Ce	28·1	23·5	16·4	9·0	15·9	12·7	13·5	13·9	17·8	13·8	18·2
Pr	4·34	3·57	2·53	1·47	2·61	2·05	2·21	2·25	2·89	2·17	3·00
Nd	21·0	17·0	12·1	7·7	13·4	10·6	11·5	11·4	14·8	10·9	15·5
Sm	6·80	5·46	3·95	2·68	4·56	3·59	3·85	3·88	4·77	3·36	5·28
Eu	1·73	1·22	1·22	0·92	1·26	1·29	1·38	1·34	1·61	1·29	1·69
Gd	8·30	6·64	4·87	3·47	5·99	4·63	5·02	5·13	6·19	4·35	6·92
Tb	1·52	1·24	0·89	0·63	1·14	0·86	0·93	0·94	1·15	0·77	1·28
Dy	9·93	8·25	5·83	4·19	7·38	5·63	6·29	6·25	7·60	5·14	8·33
Ho	2·13	1·78	1·24	0·88	1·61	1·20	1·32	1·31	1·59	1·10	1·82
Er	5·94	5·07	3·37	2·48	4·48	3·28	3·68	3·68	4·39	3·10	5·05
Tm	0·87	0·73	0·50	0·36	0·66	0·48	0·55	0·54	0·64	0·47	0·74
Yb	5·44	4·64	3·15	2·28	4·22	3·05	3·34	3·41	3·95	2·97	4·65
Lu	0·85	0·74	0·49	0·34	0·68	0·48	0·53	0·54	0·62	0·48	0·73
Hf	5·84	5·68	2·93	1·79	2·80	2·16	2·39	2·39	3·23	3·06	3·30
Pb	2·21	4·61	5·34	10·43	0·41	0·99	0·89	0·86	0·33	5·92	2·63
Th	3·67	3·42	1·24	0·48	0·84	0·62	0·67	0·82	0·90	1·61	0·86
U	1·31	1·22	0·49	0·22	0·32	0·25	0·27	0·31	0·39	0·58	0·36

(continued)

Table 2: Continued

		Unclassified lavas, hypabyssal intrusions									
Sample:	120	60A	64	66A	66B	124	36	37	38A	38B	67B
Latitude (°N):	29·90631°	29·91644°	29·92079°	29·91224°	29·91224°	29·86243°	29·88028°	29·88055°	29·88197°	29·88197°	29·91331°
Longitude (°W):	115·36240°	115·31751°	115·31029°	115·31090°	115·31090°	115·36321°	115·37385°	115·37418°	115·37493°	115·37493°	115·31058°
SiO_2	54·37	66·38	57·32	62·79	57·37	61·61	51·47	52·01	55·57	56·02	53·14
TiO_2	1·58	0·86	1·00	1·03	0·90	0·94	0·95	0·92	1·19	1·22	0·86
Al_2O_3	15·04	14·78	17·86	15·57	19·00	14·80	20·21	20·25	16·26	15·86	18·25
FeO*	12·55	6·32	8·64	3·93	5·48	7·85	9·43	9·35	11·18	11·41	8·63
MnO	0·35	0·10	0·16	0·13	0·16	0·23	0·12	0·13	0·21	0·18	0·20
MgO	4·29	1·53	2·59	1·98	2·44	2·78	3·24	3·37	4·06	3·99	5·91
CaO	7·93	4·03	7·86	7·70	7·82	6·36	10·67	10·64	7·09	6·81	9·37
Na_2O	3·23	4·95	3·51	6·23	5·99	4·26	3·49	2·89	3·84	3·65	3·05
K_2O	0·48	0·85	0·92	0·46	0·70	0·95	0·32	0·35	0·45	0·73	0·48
P_2O_5	0·19	0·22	0·14	0·18	0·14	0·21	0·11	0·10	0·14	0·14	0·11
LOI	1·78	1·06	1·01	0·31	0·60	3·73	1·35	1·57	2·30	2·96	1·87
Mg#	37·8	30·1	34·8	47·3	44·3	38·7	38·0	39·1	39·3	38·4	55·0
Rb	10·9	27·7	28·2	6·4	8·5	8·2	1·9	3·1	6·6	11·3	17·7
Sr	217	182	204	263	512	213	240	209	258	201	217
Zr	80	159	94	159	101	97	66	63	62	63	55
Ba	152	209	277	165	200	226	224	123	154	218	62
Sc	42·4	20·1	28·0	23·5	23·8	26·6	33·1	31·8	39·0	38·8	34·3
V	386	74	216	145	185	92	299	296	321	324	222
Cr	<d·l	3·1	12·7	1·4	10·9	27·1	13·4	12·6	6·4	5·7	83·7
Ni	13·99	1·67	7·19	5·98	10·52	12·81	9·50	7·92	5·64	6·93	33·79
Cu	176·1	6·4	34·7	65·1	22·7	18·2	116·0	19·8	127·7	84·0	4·2
Zn	129·3	45·5	67·3	81·5	61·6	136·9	27·6	34·1	68·5	51·2	127·8
Ga	17·4	15·9	17·2	17·7	17·9	16·0	18·5	19·6	19·0	18·0	16·8
Y	39·3	34·5	32·0	47·9	30·9	37·4	23·8	22·9	29·0	28·2	17·9
Nb	1·92	2·75	1·93	3·81	2·43	2·11	1·34	1·27	1·47	1·50	1·20
Ta	0·17	0·26	0·17	0·31	0·22	0·16	0·09	0·09	0·11	0·11	0·11
Cs	0·40	0·46	1·03	0·05	0·15	0·23	0·22	0·19	0·44	0·88	0·83
La	5·47	5·69	6·31	9·13	6·12	6·08	3·96	3·69	4·67	4·32	1·09
Ce	14·3	14·1	15·2	24·0	15·1	15·9	10·2	9·7	12·0	11·2	3·1
Pr	2·38	2·27	2·37	3·64	2·33	2·58	1·61	1·56	1·91	1·82	0·59
Nd	12·6	11·6	12·0	17·6	11·6	13·6	8·5	8·0	9·8	9·1	3·4
Sm	4·45	3·91	3·97	5·75	3·78	4·55	2·79	2·65	3·30	3·27	1·64
Eu	1·46	1·33	1·18	1·30	0·86	1·46	1·05	0·97	1·25	1·24	0·74
Gd	5·82	4·95	4·81	7·13	4·59	5·85	3·67	3·54	4·37	4·13	2·45
Tb	1·09	0·94	0·89	1·31	0·84	1·05	0·69	0·64	0·82	0·77	0·48
Dy	7·28	6·14	5·75	8·69	5·50	6·78	4·42	4·22	5·42	5·30	3·14
Ho	1·56	1·31	1·23	1·82	1·17	1·45	0·95	0·88	1·15	1·13	0·69
Er	4·38	3·74	3·43	5·22	3·34	4·07	2·64	2·51	3·14	3·15	2·00
Tm	0·64	0·55	0·50	0·77	0·50	0·60	0·39	0·37	0·47	0·46	0·30
Yb	3·98	3·50	3·12	4·84	3·18	3·78	2·43	2·28	2·91	2·96	1·88
Lu	0·65	0·55	0·50	0·74	0·50	0·60	0·38	0·36	0·46	0·47	0·31
Hf	2·62	4·68	2·79	4·50	2·90	3·07	1·98	1·87	2·04	2·03	1·62
Pb	1·48	2·79	2·63	5·92	3·80	9·28	1·13	1·05	1·55	0·76	2·03
Th	0·58	2·98	1·53	2·40	1·85	0·63	0·56	0·51	0·72	0·73	0·74
U	0·24	1·15	0·55	1·30	0·78	0·36	0·23	0·21	0·26	0·27	0·33

(continued)

Table 2: Continued

	Hornblende gabbros							Two-pyx gabbro	Mixed hybrid tonalite	Tonalites	
Sample:	73	41	46[1]	68B[1]	232[1]	63B	21B	22	23	47A	63A
Latitude (°N):	29·91161°	29·94815°	29·94368°	29·91704°	29·96298°	29·92179°	29·97127°	29·97128°	29·96913°	29·93487°	29·92179°
Longitude (°W):	115·29312°	115·32453°	115·32540°	115·30942°	115·32089°	115·31074°	115·23353°	115·24521°	115·24719°	115·32374°	115·31074°
SiO_2	51·42	53·81	50·76	53·33	50·01	59·32	57·80	52·82	61·10	64·32	65·61
TiO_2	1·25	0·81	0·51	1·17	1·12	1·07	1·02	1·00	1·19	0·87	0·92
Al_2O_3	17·34	20·26	18·68	18·07	17·98	14·76	16·67	17·51	15·87	14·76	15·04
FeO*	9·91	7·43	8·04	9·62	7·85	9·68	6·97	10·09	5·62	7·38	5·53
MnO	0·16	0·12	0·18	0·26	0·20	0·23	0·15	0·21	0·12	0·25	0·11
MgO	5·80	3·22	6·49	4·19	7·11	2·80	3·76	5·65	2·97	2·09	1·86
CaO	10·57	9·77	12·62	9·41	11·95	5·72	8·85	9·14	8·19	4·96	5·86
Na_2O	3·01	3·81	2·29	3·46	3·14	5·01	4·31	2·79	4·33	3·93	4·53
K_2O	0·37	0·67	0·38	0·37	0·49	1·26	0·34	0·70	0·38	1·28	0·34
P_2O_5	0·16	0·11	0·06	0·13	0·15	0·15	0·14	0·09	0·22	0·17	0·20
LOI	0·78	1·26	1·51	1·54	n.a	0·77	0·49	0·33	0·53	0·95	1·11
Mg#	51·1	43·6	59·0	43·7	61·8	34·0	49·0	50·0	48·5	33·5	37·5
Rb	7·8	11·2	9·6	8·7	4·5	30·0	5·4	14·4	5·4	25·4	4·6
Sr	219	262	202	226	209	162	238	212	229	198	241
Zr	66	81	25	61	51	65	103	53	105	111	181
Ba	107	174	74	133	74	299	158	209	176	328	161
Sc	36·7	30·4	52·7	33·1	38·5	42·7	31·3	32·1	27·7	24·4	23·9
V	314	231	167	275	n.a	207	262	278	193	125	110
Cr	104·0	31·2	116·0	40·7	n.a	4·2	35·2	42·7	22·8	8·2	8·7
Ni	56·15	9·31	30·09	8·47	n.a	4·21	11·29	38·41	6·24	2·07	3·53
Cu	7·3	70·9	4·4	13·5	n.a	16·8	9·3	72·6	6·0	29·0	7·7
Zn	52·7	34·8	55·4	71·8	n.a	110·5	52·2	171·5	34·2	191·6	37·6
Ga	17·2	18·7	15·2	17·8	n.a	17·0	18·6	17·7	18·2	16·2	16·5
Y	27·5	25·2	13·4	37·6	19·0	70·4	28·9	22·2	44·0	38·9	37·7
Nb	1·62	1·44	0·41	1·69	1·11	3·24	3·27	2·09	3·90	2·57	3·11
Ta	0·13	0·13	0·05	0·13	0·11	0·32	0·26	0·15	0·28	0·23	0·27
Cs	0·44	0·25	0·25	0·88	0·08	0·43	0·13	0·32	0·22	1·11	0·32
La	4·48	4·64	1·56	3·06	2·73	12·21	4·41	5·15	6·15	7·41	5·38
Ce	11·6	11·8	4·0	9·7	6·7	30·8	9·1	12·5	15·4	20·0	13·1
Pr	1·87	1·91	0·68	1·79	1·15	4·92	1·45	1·88	2·46	3·18	2·05
Nd	9·7	9·8	3·8	9·8	6·5	23·6	7·3	9·0	12·5	15·9	11·0
Sm	3·32	3·13	1·49	3·75	2·33	8·13	2·53	2·77	4·50	4·95	3·78
Eu	1·24	1·07	0·55	0·99	0·97	1·65	1·01	0·97	1·20	1·41	1·26
Gd	4·30	3·94	2·04	4·77	3·04	10·06	3·66	3·40	6·08	6·02	5·31
Tb	0·78	0·72	0·38	0·92	0·56	1·93	0·70	0·63	1·14	1·09	0·94
Dy	5·08	4·73	2·50	6·43	3·65	12·84	4·88	4·04	7·75	7·20	6·30
Ho	1·10	1·01	0·52	1·37	0·78	2·72	1·06	0·86	1·68	1·49	1·38
Er	3·08	2·79	1·47	3·95	2·09	7·72	3·01	2·42	4·69	4·17	3·89
Tm	0·45	0·40	0·21	0·62	0·31	1·16	0·45	0·36	0·70	0·62	0·60
Yb	2·74	2·54	1·30	4·02	1·85	7·17	2·95	2·31	4·39	3·84	3·78
Lu	0·44	0·37	0·21	0·65	0·28	1·16	0·48	0·36	0·71	0·63	0·62
Hf	2·07	2·37	0·80	1·89	1·48	2·88	3·02	1·62	3·28	3·44	5·28
Pb	0·91	1·68	2·41	2·16	1·30	3·64	2·15	4·89	2·28	4·23	2·28
Th	0·48	1·13	0·40	1·34	0·20	4·60	3·17	1·09	3·15	2·64	2·49
U	0·20	0·31	0·13	0·41	0·13	1·11	0·29	0·34	0·55	0·69	0·64

(continued)

Table 2: Continued

	Tonalites						Leucocratic rocks	Xenoltihs[3]			
Sample:	68A	66D2	66C	21A[2]	173	233	66D1[2]	125A	21D	48	74
Latitude (°N):	29·91704°	29·91224°	29·91224°	29·97127°	29·95079°	29·96249°	29·91224°	29·86043°	29·97127°	29·93264°	29·91241°
Longitude (°W):	115·30942°	115·31090°	115·31090°	115·23353°	115·35581°	115·31592°	115·31090°	115·36555°	115·23353°	115·32559°	115·29325°
SiO_2	70·80	63·75	67·16	66·26	67·87	66·45	70·47	67·83	56·31	59·42	59·14
TiO_2	0·69	0·87	0·75	0·85	0·64	0·81	0·51	0·82	0·90	1·30	1·66
Al_2O_3	14·31	14·59	14·65	15·92	14·89	15·26	13·35	14·81	16·66	17·01	14·21
FeO*	3·57	6·30	3·69	4·44	4·98	2·56	3·43	2·16	7·74	6·22	9·38
MnO	0·11	0·13	0·11	0·17	0·10	0·04	0·08	0·09	0·18	0·18	0·22
MgO	1·47	2·10	1·48	1·50	2·20	2·39	0·85	2·09	5·17	2·62	2·88
CaO	3·96	5·42	6·98	5·39	5·02	7·72	2·94	8·04	8·58	7·85	5·14
Na_2O	4·54	4·78	4·39	4·82	3·57	4·30	3·65	3·67	3·95	4·49	5·12
K_2O	0·44	1·89	0·63	0·64	0·64	0·30	4·62	0·33	0·40	0·73	1·85
P_2O_5	0·12	0·17	0·16	0·03	0·091	0·17	0·09	0·17	0·11	0·19	0·40
LOI	1·63	1·32	0·40	0·76	n.a	n.a	0·81	1·71	0·87	1·50	0·46
Mg#	42·3	37·3	41·7	37·5	44·0	62·5	30·5	63·3	54·3	42·9	35·3
Rb	10·4	26·8	8·7	11·7	13·1	1·1	59·4	5·1	7·5	11·7	36·1
Sr	203	174	235	246	105	102	141	307	247	314	143
Zr	173	178	197	241	125	130	188	108	65	148	266
Ba	193	638	212	325	154	9	1662	233	332	380	297
Sc	19·9	19·2	17·8	16·6	n.a	56·1	10·5	20·8	31·9	38·2	32·3
V	49	103	87	172	n.a	n.a	54	129	244	110	195
Cr	5·5	7·9	6·7	5·7	n.a	n.a	5·5	12·1	60·6	<d·l	<d·l
Ni	0·39	4·63	3·35	3·96	n.a	n.a	1·58	2·96	31·19	0·49	1·58
Cu	12·4	5·5	38·9	19·4	n.a	n.a	6·0	3·6	14·4	16·2	3·2
Zn	168·0	25·5	129·7	24·9	n.a	n.a	20·2	32·3	51·3	103·8	60·6
Ga	15·3	16·2	14·6	18·2	n.a	n.a	13·6	15·6	19·4	18·5	19·2
Y	43·6	55·6	36·1	12·6	38·1	25·4	19·7	27·3	31·2	59·5	59·6
Nb	3·00	3·67	3·11	2·34	3·05	0·57	2·68	2·22	2·65	3·23	6·49
Ta	0·28	0·26	0·29	0·23	0·25	0·13	0·31	0·17	0·20	0·26	0·50
Cs	0·26	0·45	0·21	0·17	0·08	0·07	0·21	1·97	0·37	0·34	0·68
La	7·59	6·25	7·74	4·27	8·85	1·52	3·31	6·36	4·72	9·88	15·58
Ce	25·2	16·5	18·3	7·3	21·9	4·8	8·0	15·3	12·0	29·4	39·4
Pr	4·58	2·75	2·65	1·01	3·37	0·84	1·28	2·02	1·95	4·78	5·97
Nd	24·6	14·5	12·7	4·5	16·3	4·3	6·4	9·5	9·8	23·8	28·8
Sm	7·62	5·40	4·10	1·22	5·19	1·49	2·16	3·02	3·20	7·19	8·38
Eu	1·93	1·84	1·59	1·23	1·64	0·37	0·99	1·39	1·16	1·96	2·11
Gd	8·46	7·31	5·11	1·55	5·86	2·25	2·73	4·07	4·23	8·98	9·63
Tb	1·38	1·40	0·94	0·29	1·06	0·47	0·50	0·75	0·81	1·63	1·70
Dy	8·47	9·44	6·06	1·97	6·78	3·57	3·19	4·81	5·54	10·72	10·92
Ho	1·76	2·02	1·32	0·45	1·45	0·87	0·72	1·05	1·20	2·28	2·33
Er	4·89	5·90	3·83	1·37	4·27	2·85	2·12	2·92	3·49	6·40	6·56
Tm	0·72	0·89	0·57	0·20	0·64	0·49	0·33	0·43	0·53	0·92	0·97
Yb	4·48	5·56	3·64	1·45	4·15	3·60	2·21	2·65	3·42	5·70	6·07
Lu	0·68	0·86	0·59	0·25	0·66	0·71	0·38	0·43	0·56	0·86	0·96
Hf	5·37	5·20	5·93	5·92	3·53	3·92	6·01	3·12	1·98	4·49	7·10
Pb	2·14	1·21	1·61	1·66	1·00	5·66	1·72	2·64	2·06	2·17	0·52
Th	5·64	3·03	3·59	0·98	1·01	2·13	6·81	0·73	1·57	2·60	2·83
U	2·18	1·38	1·02	0·31	0·47	0·96	2·07	0·25	0·32	0·81	1·03

Major elements normalized to 100 wt.% on a volatile-free basis. LOI values are provided for information only. FeO* is total FeO. Non-primary or cumulate samples include: [1]hornblende cumulates, [2]plagioclase cumulates (felsic), and [3]xenoliths, and were not included in major, minor and trace element plots. Underlined sample is affected by accessory phase, and is omitted from minor and trace element plots. ICP-MS data is presented for trace elements, with the exception of Zr and Rb where XRF data is presented (see Electronic Appendix 1). <d.l indicates less than detection limit. n.a. indicates data not analyzed.

for ICP-MS-analyzed trace elements are: <30 ppm for Ba; ≤10 ppm for Sr and Zr; ≤2 ppm for Rb, Sc, and Y; ≤1 ppm for Ce, Nd, and Dy; ≤0·5 ppm for La, Pr, Sm, Eu, Gd, Tb, Ho, Er, Yb, Th, Nb, Hf, and Pb; and ≤0·1 ppm for Tm, Lu, Ta, U, and Cs. Precision estimates measured between repeat samples at WSU were ≤2·5%. Duplicate samples (both XRF and ICP-MS data) were submitted externally and measured differences are discussed in Supplementary Data Electronic Appendix 1.

Twenty-four samples, representative of each lithological unit, were analyzed for Sr, Nd, and Pb isotope ratios (Table 3). Least altered samples were chosen based on thin section petrography. Approximately 0·5–0·7 g of rock powder was prepared at WWU using a silica mortar and pestle, which was decontaminated between samples. Powders were submitted to the University of Washington where column chemistry was completed on all the samples prior to analysis. Analyses were completed using a Nu multi-collector ICP-MS at the University of Washington as per analytical methods described by Gaffney *et al.* (2007), Harkins *et al.* (2008), and Brach-Papa *et al.* (2009). The following standards were used to normalize measured isotopic ratios: NBS 987 for $^{87}Sr/^{86}Sr$ (0·710240), La Jolla for $^{143}Nd/^{144}Nd$ (0·511843), and NIST-981 for $^{208}Pb/^{204}Pb$ (36·721), $^{207}Pb/^{204}Pb$ (15·491), and $^{206}Pb/^{204}Pb$ (16·937). The external reproducibility at $\pm 2\sigma$ for samples analyzed are Nd = ±30 ppm; Sr = ±40 ppm; and Pb = ±125, 150, and 200 ppm for $^{206}Pb/^{204}Pb$, $^{207}Pb/^{204}Pb$ and $^{208}Pb/^{204}Pb$, respectively (Table 3).

Mineral chemistry

Minerals were analyzed for major element chemistry by electron probe micro analysis (EMPA) using a four-wavelength spectrometer JEOL 733 Superprobe at the University of Washington (Supplementary Data Electronic Appendix 2, Tables S1A–S1E). Instrument conditions were set for specific minerals: pyroxene, amphibole, biotite, plagioclase, and Fe–Ti oxides, which were measured using a 15 kV accelerating potential and either a 10 nA (pyroxene, amphibole, biotite) or a 20 nA (plagioclase, Fe–Ti oxides) beam current. A focused beam diameter of <1 μm was set for all minerals excluding plagioclase, for which the beam diameter was set at 3 μm. Element peaks and backgrounds were counted for 40 s for all elements, with the exception of Fe and Sr in plagioclase (130 s and 100 s respectively). Analytical error is <3% for major elements and <8% for minor elements. Analytical error is higher for element oxides present in trace concentrations <1 wt %. Corrections for Fe–Ti oxide mineral chemistry were required for FeO_{total} and TiO_2 wt %. Fe–Ti oxides were adjusted for small, consistent differences observed in the Elba hematite and synthetic rutile standards used at the University of Washington. Methods for these FeO_{total} and TiO_2 corrections are outlined by Evans *et al.* (2006).

Amphibole trace element chemistry was analyzed from hornblende gabbro, hornblende cumulate, two-pyroxene gabbro, and mixed hybrid tonalite samples via laser ablation inductively coupled plasma mass spectrometry (LA-ICP-MS) at the University of Calgary (Supplementary Data Electronic Appendix 2, Table S2). These grain analyses include both primary amphibole (magnesio-ferri-hornblende and magnesio-hornblende) and secondary actinolitic amphibole. Analyses were conducted using an Agilent 7700 quadrapole ICP-MS coupled with an ASI Resochron 193 nm Excimer UV laser, using a helium flow-through sample cell. The laser was set at a repetition rate of 10 Hz and fluence of 1·0 J cm^{-2}, ablating spot sizes were ~50 μm in diameter. NIST 610 was used as the internal standard and previously measured CaO wt % from EMPA analyses was used as the external standard. Data reduction was completed at the University of Calgary using the Iolite™ (V2.5) software package (Paton *et al.* 2010) and the VizualAge data reduction scheme (Petrus & Kamber, 2012). Analyzed elements, and their respective averaged detection limits include: ^{39}K (1·87 ppm), ^{44}Ca (52·19 ppm), ^{47}Ti (0·098 ppm), ^{85}Rb (0·080 ppm), ^{88}Sr (0·045 ppm), ^{89}Y (0·058 ppm), ^{90}Zr (0·041 ppm), ^{93}Nb (0·037 ppm), ^{137}Ba (0·083 ppm), ^{139}La (0·040 ppm), ^{140}Ce (0·042 ppm), ^{141}Pr (0·035 ppm), ^{146}Nd (0·059 ppm), ^{147}Sm (0·055 ppm), ^{153}Eu (0·041 ppm), ^{157}Gd (0·059 ppm), ^{159}Tb (0·033 ppm), ^{163}Dy (0·041 ppm), ^{165}Ho (0·033 ppm), ^{166}Er (0·040 ppm), ^{169}Tm (0·032 ppm), ^{172}Tb (0·043 ppm), ^{175}Lu (0·032 ppm), and ^{181}Ta (0·033 ppm).

Geochronology

$^{40}Ar/^{39}Ar$ incremental heating experiments were conducted on both groundmass and plagioclase separates using a 25 W CO_2 laser, and the gas was analyzed using the single-collector MAP215-50 mass spectrometer in the WiscAr Laboratory at the University of Wisconsin–Madison (Jicha & Brown, 2014). Five new ages are calculated using a Fish Canyon Tuff sanidine age of 28·201 ± 0·046 Ma (Kuiper *et al.*, 2008) and the decay constants of Min *et al.* (2000). Complete Ar isotope data are available in Supplementary Data Electronic Appendix 3 (Table S3).

WHOLE-ROCK CHEMISTRY

Samples are identified in the following text and figures as simplified lithological groups: (1) plutonic rocks (comprising tonalite, hornblende gabbro, two-pyroxene gabbro, mixed hybrid tonalite, hornblende-bearing enclaves, and leucocratic rocks); (2) hypabyssal intrusions; (3) lavas, and block-and-ash-flow tuffs (lavas, and B & AFTs in figures); (4) ignimbrites; and (5) unclassified volcanic rocks, which may include lavas, hypabyssal intrusions, and fine-grained xenoliths within plutons (unclassified in figures). Samples generally referred to as 'volcanic rocks' include the latter four groups. Fine-grained volcaniclastic rocks were not sampled for major

Table 3: Isotope and trace element data

Rock type	Sample	$^{87}Rb/^{86}Sr$	$^{147}Sm/^{144}Nd$	$^{87}Sr/^{86}Sr$	$^{143}Nd/^{144}Nd$	$^{206}Pb/^{204}Pb$	$^{207}Pb/^{204}Pb$	$^{208}Pb/^{204}Pb$	$Sr_{(i)}$ (110 Ma)	$Nd_{(i)}$ (110 Ma)	ε_{Nd} (110 Ma)	$^{206}Pb_{(i)}$ (110 Ma)	$^{207}Pb_{(i)}$ (110 Ma)	$^{208}Pb_{(i)}$ (110 Ma)
Ignimbrite	35A	0·151133	0·1950	0·705280	0·51296	18·54	15·57	38·24	0·705044	0·51282	+6·39	18·45	15·56	38·17
Lavas	34	0·179365	0·2027	0·705150	0·51300	18·53	15·56	38·22	0·704869	0·51285	+6·89	18·49	15·56	38·19
	80	0·583449	0·1618	0·706030	0·51290	19·42	15·61	39·00	0·705117	0·51279	+5·67	18·12	15·55	37·98
	106	0·197089	0·2044	0·704893	0·51296	18·88	15·60	38·48	0·704584	0·51281	+6·17	18·38	15·57	38·09
Volcaniclastic rock	26B	0·320542	0·1684	0·706029	0·51292	20·61	15·68	39·63	0·705528	0·51280	+5·98	18·57	15·58	38·22
Hypabyssal intrusions	25	0·523784	0·1942	0·705590	0·51294	19·42	15·64	38·95	0·704771	0·51280	+5·84	19·12	15·63	38·68
	29	0·098610	0·1971	0·704070	0·51296	18·56	15·56	38·25	0·703916	0·51282	+6·31	18·46	15·56	38·17
	70C	0·153178	0·1871	0·704031	0·51298	18·58	15·57	38·29	0·703791	0·51285	+6·83	18·47	15·56	38·19
	125B	0·063399	0·2090	0·705093	0·51298	18·50	15·56	38·20	0·704994	0·51283	+6·52	18·48	15·56	38·18
	108	0·134638	0·2063	0·705431	0·51300	19·08	15·59	38·69	0·705220	0·51285	+6·94	18·21	15·55	37·94
	118	0·136717	0·2065	0·704030	0·51297	18·62	15·57	38·29	0·703817	0·51283	+6·41	18·47	15·57	38·17
Unclassified rocks*	64	0·398962	0·2004	0·704403	0·51299	18·72	15·58	38·39	0·703779	0·51284	+6·73	18·49	15·56	38·18
	124	0·110877	0·2022	0·704758	0·51298	18·52	15·56	38·20	0·704585	0·51283	+6·61	18·47	15·56	38·18
	37	0·042281	0·2003	0·703997	0·51300	18·66	15·58	38·32	0·703931	0·51285	+6·95	18·44	15·57	38·15
	67B	0·235958	0·2884	0·704196	0·51304	18·63	15·57	38·32	0·703827	0·51283	+6·52	18·46	15·56	38·18
Plutonic rocks	47A	0·370247	0·1890	0·704645	0·51298	18·85	15·57	38·47	0·704066	0·51284	+6·77	18·67	15·56	38·24
	63A	0·055567	0·2080	0·704228	0·51301	18·71	15·57	38·58	0·704142	0·51286	+7·09	18·40	15·56	38·19
	66D2	0·444925	0·2247	0·705800	0·51300	19·57	15·62	39·03	0·705105	0·51284	+6·69	18·30	15·56	38·12
	73	0·103019	0·2068	0·703920	0·51296	18·64	15·59	38·32	0·703759	0·51281	+6·15	18·40	15·57	38·13
	22	0·196359	0·1863	0·703818	0·51297	18·56	15·56	38·27	0·703511	0·51284	+6·70	18·49	15·56	38·19
Cumulates	21A	0·138087	0·1635	0·704303	0·51294	18·65	15·58	38·41	0·704087	0·51283	+6·45	18·45	15·57	38·20
	46	0·137133	0·2350	0·703942	0·51301	18·57	15·57	38·28	0·703728	0·51285	+6·82	18·51	15·57	38·22
Xenolith	125A	0·048297	0·1927	0·704568	0·51298	18·57	15·56	38·27	0·704493	0·51284	+6·80	18·47	15·56	38·17
Stoped block	48	0·108335	0·1825	0·704798	0·51298	18·82	15·59	38·56	0·704629	0·51285	+6·90	18·40	15·57	38·13

*Unclassified lavas or hypabyssal intrusions.

Age of rocks (110 Ma) is based on zircon ages from Busby *et al.* (2006) and $^{40}Ar/^{39}Ar$ ages from this study. $Sr_{(i)}$, $Nd_{(i)}$, $^{206}Pb_{(i)}$, $^{207}Pb_{(i)}$, and $^{208}Pb_{(i)}$ refer to initial $^{87}Sr/^{86}Sr$, $^{143}Nd/^{144}Nd$, $^{206}Pb/^{204}Pb$, $^{207}Pb/^{204}Pb$, and $^{208}Pb/^{204}Pb$, respectively. Initial CHUR values [for $\varepsilon_{Nd\ (110\ Ma)}$] were calculated using present-day values of $^{143}Nd/^{144}Nd = 0{\cdot}512638$ and $^{147}Sm/^{144}Nd = 0{\cdot}1967$ (Goldstein *et al.*, 1984; Peucat *et al.*, 1988). External reproducibility at 2σ is Nd = ±30 ppm, Sr = ±40 ppm, and Pb = ±125, 150 and 200 ppm for $^{206}Pb/^{204}Pb$, $^{207}Pb/^{204}Pb$, and $^{208}Pb/^{204}Pb$, respectively.

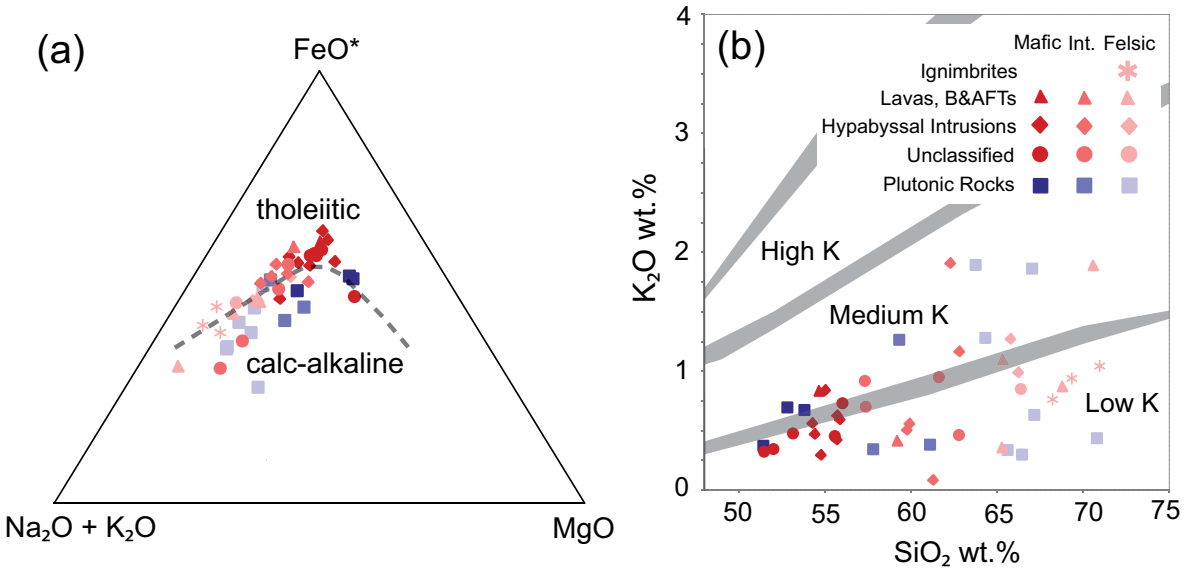

Fig. 5. Whole-rock major element characteristics of the sample suite. (a) AFM (alkali–iron–magnesium) diagram as defined by Irvine & Baragar (1971). FeO* is FeO_{total}. Samples display transitional tholeiitic to calc-alkaline character. (b) K_2O vs SiO_2 diagram, with most samples plotting in the low-K field. Compositional fields are defined by the boundary lines of Gill (1981).

and trace element geochemical analyses given the lack of clarity about their source regions; however, isotope ratios are presented for one volcaniclastic sample (26B) for comparison (described below).

Samples are plotted in Figs 5–8, where dark to light shaded colors differentiate between mafic samples (<57 wt % SiO_2), intermediate samples (57–63 wt % SiO_2), and felsic samples (>63 wt % SiO_2) (Le Maitre, 1989). To clearly discern liquid lines of descent on these plots, obvious plutonic cumulate (i.e. plagioclase and hornblende cumulates) and xenolith samples are omitted. Samples whose trace element signatures are clearly affected by accessory-phase minerals (i.e. titanite) are omitted from trace element plots (Figs 7 and 8).

Major and trace element chemistry

Plutonic and volcanic units display transitional tholeiitic to calc-alkaline character (Fig. 5a; Irvine & Baragar, 1971). Samples that plot squarely on the tholeiitic side are predominantly aphyric basaltic andesite samples (106, 118, 120), which include both lava and sill units. All samples are low- to medium-K, with most plotting in the low-K field (Fig. 5b; Le Maitre, 1989). Low K values are not attributed to alteration (no correlation between K_2O and LOI), with the exception of two dikes (28B and 28C) that have high LOI (>5%) and low K. These small-scale (1–2 m wide) dikes may have been subject to hydrothermal alteration along dike margins.

Plutonic and volcanic rocks range in composition from 51 to 71 wt % SiO_2 and from 5·9 to 0·9 wt % MgO, with the majority of the volcanic rocks being basaltic andesite to dacite (Figs 6 and 7). Outliers include volcanic samples (28A and 66B) that plot as basaltic trachyandesite and trachyandesite, respectively, where elevated Na_2O wt % is likely due to albitization of plagioclase. Leucocratic rocks have granite to granodiorite modal compositions, but show feldspar-cumulative chemistry, and are not included in the geochemical plots.

Harker diagrams (Figs 6 and 7) display remarkable overlap in composition between plutonic and volcanic samples (51·4–70·8 wt % SiO_2 for plutonic samples compared to 51·5–71·0 wt % SiO_2 for volcanic samples). Samples exhibit decreasing trends of TiO_2, Al_2O_3, FeO_{total}, MgO, and CaO wt % relative to SiO_2 wt %, with a slight inflection at 63 wt % SiO_2, observable in TiO_2, MgO, and Al_2O_3 wt %. Both K_2O and NaO wt % increase with increasing SiO_2 wt % (Figs 5b and 6f). MnO and P_2O_5 are present in low concentrations (<0·5 wt %) for all samples (not plotted).

Bivariate plots of trace elements show moderately increasing Ba, Y, Zr, Nb, La, and Yb (Y and Nb not shown) with increasing SiO_2, but a concomitant decrease in Sr (Fig. 7b). Cr and Ni show expected decreasing trends relative to SiO_2. A strong inflection at 63 wt % SiO_2 is visible in the trends for Zr, Nb, La, and Yb. Between 61–64 SiO_2 wt %, a subset of five samples (plutonic, hypabyssal, and unclassified volcanic) show distinctly higher abundances of these elements than the inflected trend. The Zr and Yb vs SiO_2 wt % plots suggest that there could be two trends, a higher and a lower one.

Chondrite-normalized REE trends show flat patterns with $La/Yb_{(N)}$ ~1·0–1·5 (0·8–1·6 for plutonic rocks; 1·0–1·5 for volcanic rocks) (Fig. 8a and b). There is remarkable REE overlap between plutonic and volcanic

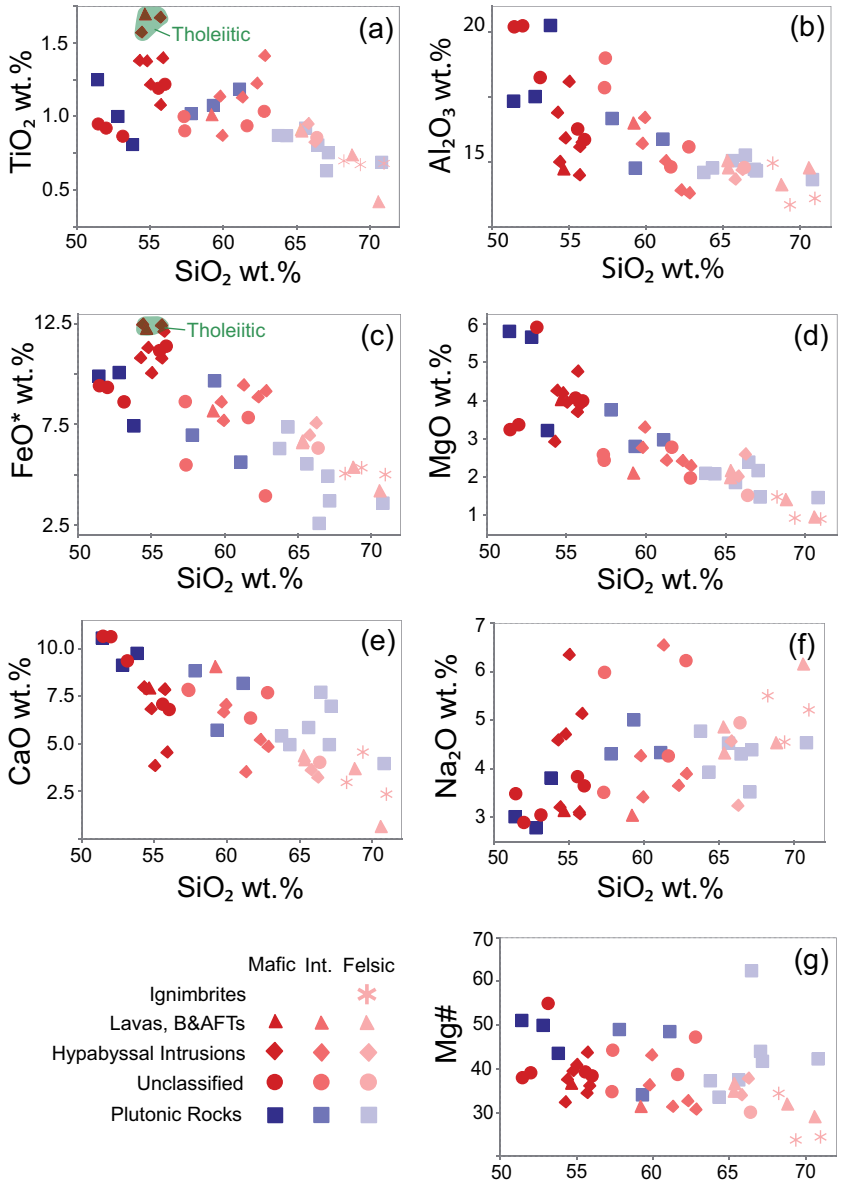

Fig. 6. Whole-rock major element variation diagrams for plutonic (blue shade) and volcanic (red to pink shade) rocks. No obvious cumulate samples or xenoliths are plotted. Trends of plutonic and volcanic rocks display compositional overlap. Slight inflections ~63 wt % SiO_2 are observed in TiO_2, MgO, and Al_2O_3. Some basaltic-andesite samples with tholeiitic affinities have elevated FeO* (FeO_{total}) and TiO_2.

samples (see Fig. 8a and b insets); however, volcanic samples display a greater range in abundances. Tholeiitic basaltic andesite samples have elevated middle REE (MREE) and heavy REE (HREE) abundances compared to most other samples. Samples with tholeiitic affinities are apparent in select bivariate plots, such as FeO_{total} and TiO_2 vs SiO_2 (Fig. 6a and c), and Yb vs SiO_2 (Fig. 7d). REE abundances increase from mafic to intermediate compositions for both plutonic and volcanic samples, but that increase does not continue with felsic compositions (see plots of La and Yb vs SiO_2 in Fig. 7c and d). Samples with >63 wt % SiO_2 instead show scatter of REE with SiO_2. Eu anomalies (Eu/Eu*) are similar in size between plutonic and volcanic units and are generally negative (<1) for mafic (0·74–1·03), intermediate (0·62–1·03), and felsic (0·70–1·06) samples (Fig. 8a and b).

Extended trace element plots show large ion lithophile element (LILE) enrichment and high field strength element (HFSE) depletion, typical of arc settings (Pearce & Peate, 1995) (Fig. 8c and d). As with the REE, there is remarkable trace element overlap between plutonic and volcanic samples (see Fig. 8c and d insets); however, volcanic samples generally display a greater range in

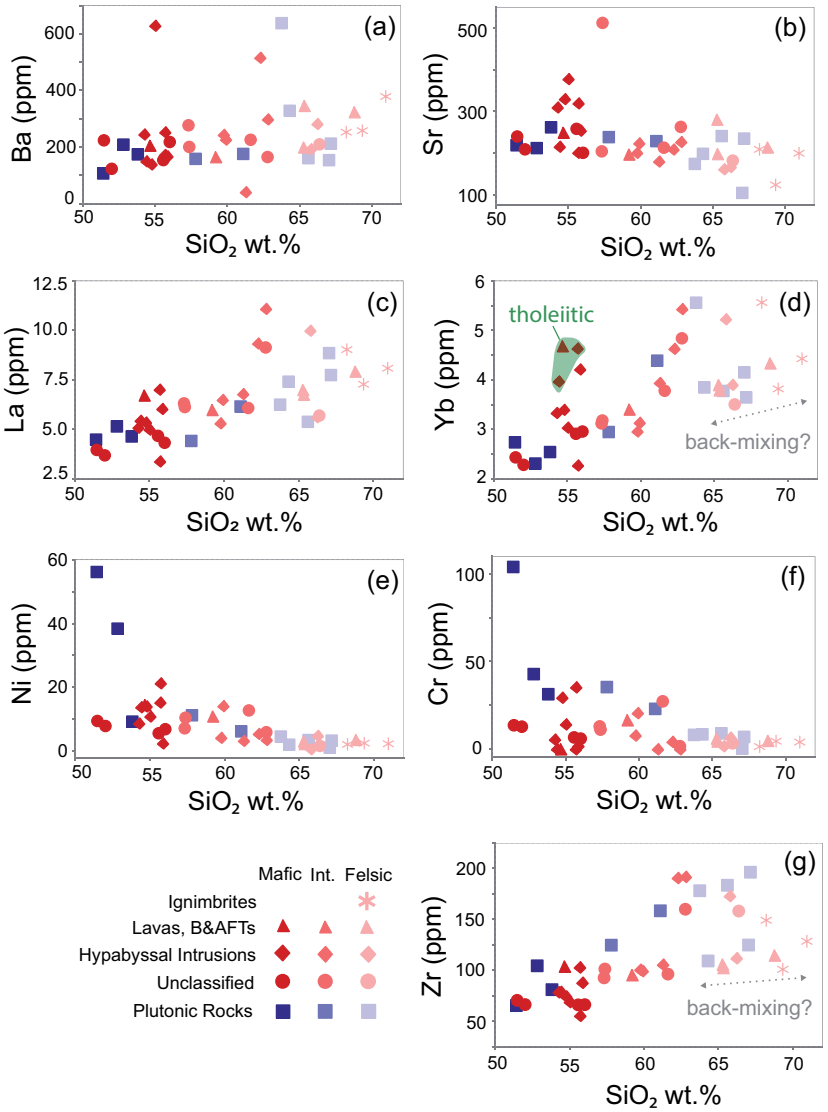

Fig. 7. Whole-rock trace element variation diagrams for plutonic (blue shade) and volcanic (red to pink shade) rocks. No obvious cumulate samples or xenoliths are plotted. Samples affected by accessory-phase minerals are omitted from plot. Plots show moderate increases in Ba, Zr, La, and Yb, and a decrease in Sr with increasing wt % SiO_2. Inflections ~63 wt % SiO_2 are visible in trends for Zr, La, and Yb. Some basaltic-andesite samples with tholeiitic affinities have elevated MREE and HREE abundances compared to the other samples (see Yb vs SiO_2 plot). Zr and Yb vs SiO_2 wt % plots suggest that there could be two trends, a higher and a lower one.

LILE and HFSE. Overall, incompatible trace elements display trends of increasing abundances from mafic to intermediate compositions (Figs 7 and 8). Intermediate and felsic compositions have higher abundances than mafic compositions, with limited crossing patterns.

Isotope chemistry

Initial isotopic ratios (Sr_i, Nd_i, Pb_i) for samples from all lithological groups, as well as cumulates, xenoliths, and one volcaniclastic rock, are shown in Table 3 and Fig. 9. Ratios were calculated using an average age of 110 Ma based on zircon ages from Busby *et al.* (2006), and $^{40}Ar/^{39}Ar$ ages (113·9–106·4 Ma) from this study (discussed below). The uniformity in Nd_i ratios is especially striking; all are within the range of 0·51279–0·51286 ($\varepsilon_{Nd} = 5{\cdot}7–7{\cdot}1$) (Fig. 9a) displaying no co-variation between ε_{Nd} and wt % SiO_2 or any incompatible trace element. There is a greater variation in Sr_i ratios (0·7035–0·7055), where ratios display a positive correlation with LOI wt %, but not with SiO_2 wt % (plots not shown). Overall, isotope ratios show no systematic difference between plutonic and volcanic samples.

The limited range in Nd_i ratios and lack of correlation with SiO_2 provides evidence for this entire segment of the arc to be derived from a uniform mantle source, with any incorporated crust necessarily being isotopically similar to the parental magma. The positive correlation between Sr_i ratios and LOI indicates that the variation is due to alteration. Alteration-related variability is the most likely explanation for the contrast

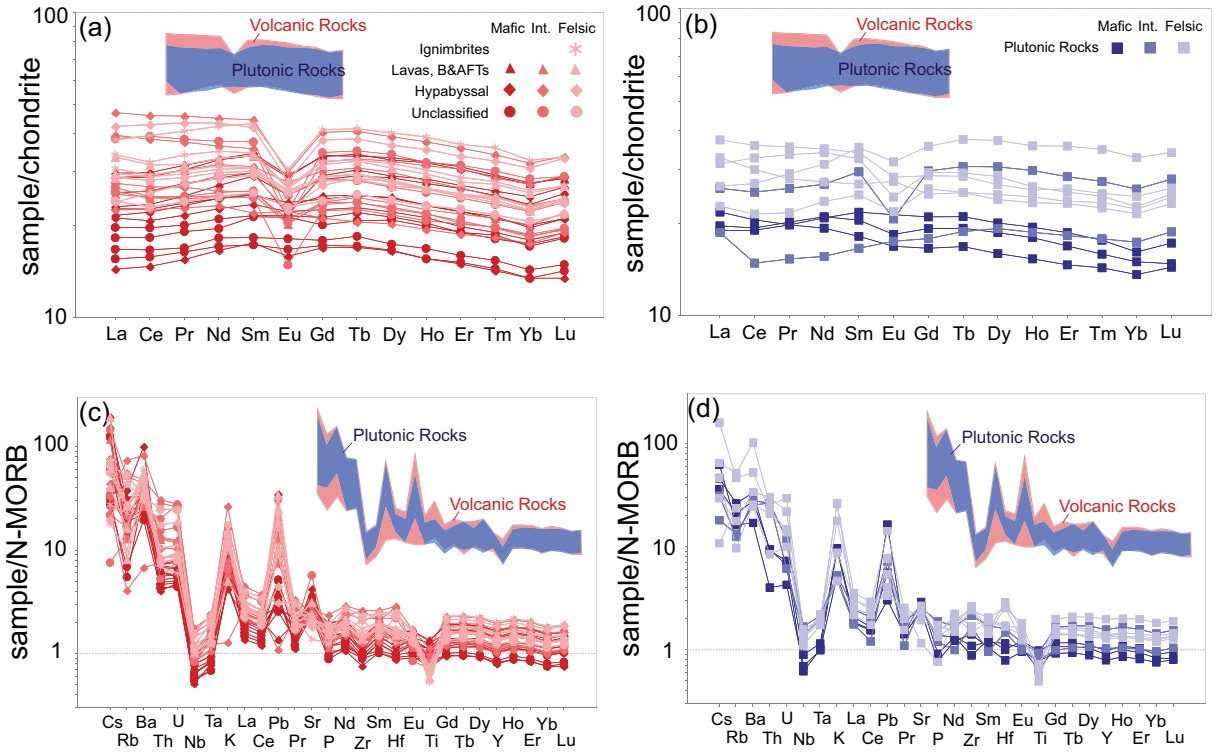

Fig. 8. Whole-rock trace element pattern comparison between plutonic and volcanic units. Chondrite-normalized REE plots (Sun & McDonough, 1989) show remarkable overlap between (a) volcanic and (b) plutonic units (see insets), although volcanic units extend to higher abundances. N-MORB-normalized extended trace element plots (Sun & McDonough, 1989) for (c) volcanic and (d) plutonic units display LILE enrichment and HFSE depletion. Insets show that volcanic and plutonic units overlap, although volcanic units have a greater range in LILE and HFSE.

between Sr_i ratios observed in neighboring samples that have similar geochemical compositions, and are likely similar in origin and timing based on field relationships (i.e. samples 108 and 118, with Sr_i of 0·7052 and 0·7038, respectively). Hydrothermal alteration can contribute to higher Sr_i ratios, but is less likely to affect Nd_i ratios.

Plutonic and volcanic rocks display similar initial Pb_i ranges, with volcanic units displaying the greatest range for all Pb_i ratios (Fig. 9b, Table 3). All samples plot above the Northern Hemisphere Reference Line (NHRL) (Fig. 9b). There is no correlation of any of the Pb_i isotope ratios with LOI, SiO_2, or any incompatible trace element.

Three samples that were analyzed to assess any variation in crustal input (a volcanic stope block, a tonalite xenolith, and a mafic volcaniclastic rock) all plot within the isotopic ranges of the plutonic and volcanic rocks, except for the Sr_i of the volcaniclastic rock (26B), which plots at the upper end (0·7055).

$^{40}Ar/^{39}Ar$ geochronology

We report results of five new $^{40}Ar/^{39}Ar$ ages on the volcanic section (locations shown in Fig. 1b). Groundmasses were analyzed for most of the samples because they are aphyric, with the exception of plagioclase from a phyric andesite block-and-ash-flow tuff (sample 30, block sampled). $^{40}Ar/^{39}Ar$ plateau ages (Supplementary Data Electronic Appendix 3) appear to form two age clusters. The older age cluster includes: (1) sample 19, basaltic andesite lava, with an age of 113·9 ± 1·3 Ma; (2) sample 30, andesite plagioclase-phyric block-and-ash-flow tuff, with an age of 111·1 ± 2·7 Ma; and (3) sample 161, basaltic andesite lava, with an age of 110·6 ± 2·0 Ma. The younger cluster includes: (1) sample 141, basaltic andesite lava, with an age of 106·4 ± 0·6 Ma; and (2) sample 120, basaltic andesite sill, with an age of 107·6 ± 0·7 Ma. The older ages come from the upper part of the section in the northern fault-bounded basin (sample 19), the top of the section in the southern volcano-bounded basin (sample 30), and the middle of the section in the central subaerial edifice (sample 161). The two younger ages come from the top of the section in the central subaerial edifice (sample 141), and from a sill in the southern volcano-bounded basin (sample 120). When considering the age uncertainties, the oldest calculated age on the younger cluster (108·3 Ma) is only 0·1 Myr younger than the

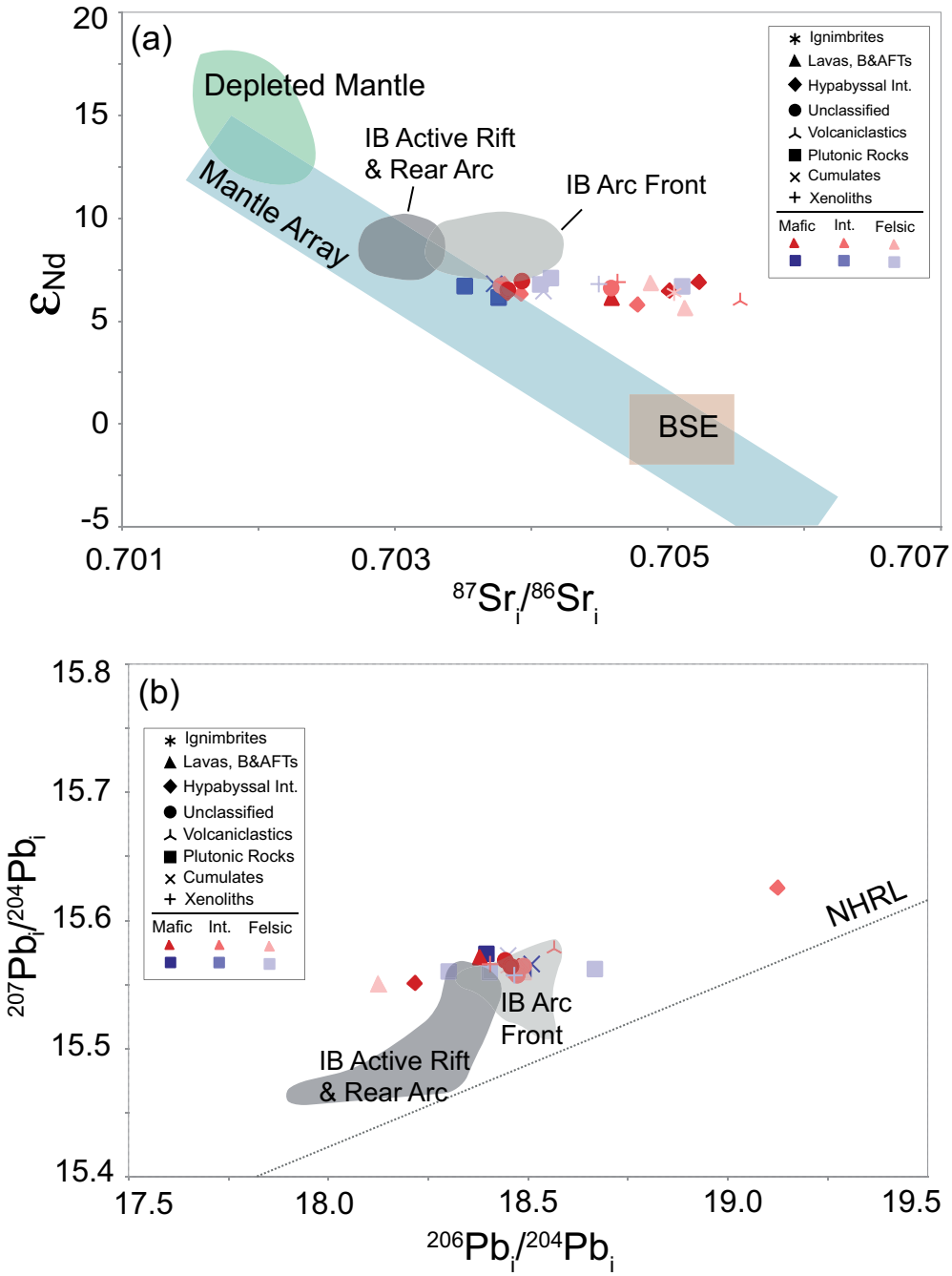

Fig. 9. Initial isotopic systematics for southern volcano-bounded basin samples corrected to 110 Ma from Busby *et al.* (2006) and $^{40}Ar/^{39}Ar$ ages from this study. Data from the Izu–Bonin (IB) arc are plotted for comparison (see text for discussion) (Hochstaedter *et al.*, 2001; Tollstrup *et al.*, 2010). The Izu–Bonin rear arc consists of backarc knolls and western seamounts (Heywood, 2018). (a) ε_{Nd} vs $^{87}Sr_i/^{86}Sr_i$. The limited range in ε_{Nd} shows that plutonic and volcanic samples evolved as a closed system fed from one subduction-modified mantle source, with no contribution from old cratonic crust. Variability in Sr_i ratios is likely due to hydrothermal alteration. BSE indicates 'Bulk Silicate Earth'. (b) $^{207}Pb_i/^{204}Pb_i$ vs $^{206}Pb_i/^{204}Pb_i$ showing a limited range of values that do not correspond with wt % SiO_2. The Northern Hemisphere Reference Line (NHRL) is defined by Hart (1984).

youngest calculated age on the older cluster (108·4 Ma). However, the ages taken together cover a timespan of ~7·5 ± 1·9 Myr. The ages are consistent with multigrain U–Pb zircon ages of ~110–111 Ma reported by Busby *et al.* (2006), but cover a longer time span. The $^{40}Ar/^{39}Ar$ ages agree well with a mid-Albian (110–107·6 Ma) age recently assigned to Alisitos gastropod species by Squires (2018), where most ages span the Early to mid-Albian (113–107·6 Ma) (Gradstein *et al.*, 2012).

DISCUSSION

The limited range in initial ε_{Nd} values from basaltic to rhyolitic compositions in the southern volcano-

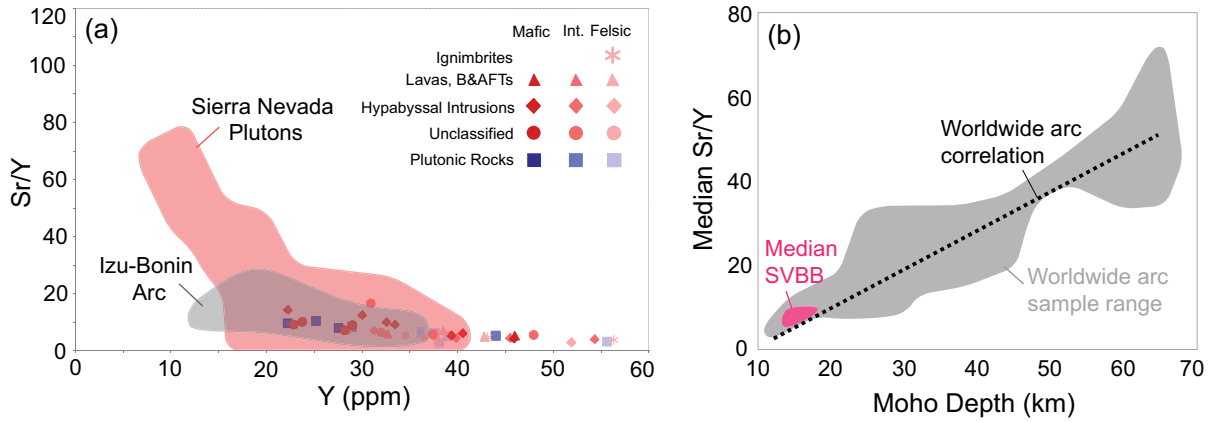

Fig. 10. (a) Plot of Sr/Y vs Y compared with Izu–Bonin arc volcanic rocks (Hochstaedter *et al.*, 2001; Tollstrup *et al.*, 2010) and northern Sierra Nevada plutonic rocks (Cecil *et al.*, 2012). Low Sr/Y ratios of <20 indicate the arc did not have a deep crustal root that stabilized garnet. (b) Sr/Y of southern volcano-bounded basin samples (SVBB) plotted on worldwide arc correlation of Sr/Y with crustal thickness (from Chapman *et al.*, 2015). Low (5–10) median Sr/Y ratios indicate a thin crust with <20 km Moho depth. Low (<0·6) Ce/Y ratios (not shown) also indicate a thin crust with ratios similar to other oceanic extensional arcs (Mantle & Collins, 2008).

bounded basin provides critical evidence that the arc crust (both the plutonic roots and the erupted volcanics) developed as a closed system fed by a uniform subduction-modified mantle source, with no contribution from old continental crust (Fig. 9a). These Nd isotopic values are lower than typical normal mid-ocean ridge basalt (N-MORB), but still fall within the range of oceanic arcs that do not have a continental basement, such as the Mariana arc (Sun & Stern, 2001).

The lack of extensive cratonic basement beneath this segment of the Alisitos arc is also supported by low Sr/Y ratios of <20 (Fig. 10) and Ce/Y ratios of <0·6 (not shown). These ratios have been used to infer crustal thickness (Mantle & Collins, 2008; Cecil *et al.*, 2012; Chapman *et al.*, 2015; Lieu & Stern, 2019). When plotted on the empirical worldwide arc correlation of Chapman *et al.* (2015), the Alisitos Sr/Y ratios fall on the thinnest end of the spectrum, suggesting that its crust was <20 km thick. These ratios, as well as others such as Dy/Yb, support the fact that the Alisitos arc did not have a deep crustal root that stabilized garnet (see Mantle & Collins, 2008; Chapman *et al.*, 2015).

An outstanding question, however, is how much within-arc recycling of magmatic components was responsible for the range of compositions present. Is closed-system fractional crystallization sufficient to produce the observed trends? Or is some concomitant melting of the older roots of the volcanic system allowable or necessary?

Magma differentiation—what processes are responsible?

Our goal in the following section is to decipher the differentiation processes responsible for the evolution of basaltic andesite to rhyolite compositions in the southern volcano-bounded basin arc segment. We show the details of how closed-system fractional crystallization of a basaltic andesite parental magma can produce most of the evolved compositions, but trace element abundances of dacite and rhyolite are not explainable by simplified fractionation models.

To fully decipher differentiation processes, the following sections outline features of crystallization order (e.g. timing of hornblende crystallization), the choice of starting composition, the results of major element modeling using MELTS and a simple subtraction model, and the results of trace element modeling. This is followed by a discussion of the implications of the modeling results.

Timing of hornblende crystallization

The timing of hornblende crystallization is important for interpreting magma evolution, as its distinct chemical composition affects magma geochemical trends during crystallization. Hornblende is rare in volcanic units, but it is abundant in plutonic rocks. Petrographic observations of the plutonic rocks, especially of hornblende gabbro, support late-stage crystallization, where anhedral hornblende has crystallized between euhedral plagioclase grains.

Hornblende gabbros contain plagioclase that displays early calcic cores (An# >90) with more sodic rims (An# 48). These plagioclase rims are in equilibrium with neighboring hornblende (i.e. sample 46, Supplementary Data Electronic Appendix 2), thus the more calcic plagioclase is a remnant of much earlier crystallization. Strong negative Eu anomalies in the REE patterns of hornblende (Fig. 11) also indicate that it must have begun crystallizing well after plagioclase.

Most hornblende displays expected MREE enrichment (Tiepolo *et al.*, 2007; Nandedkar *et al.*, 2016) but interestingly, two-pyroxene gabbroic samples display hornblende REE patterns more typical of pyroxene, as indicated by their smaller positive-sloping light REE (LREE) patterns from La to Pr (e.g. Greene *et al.*, 2006) (Fig. 11). Prior fractionation of orthopyroxene and

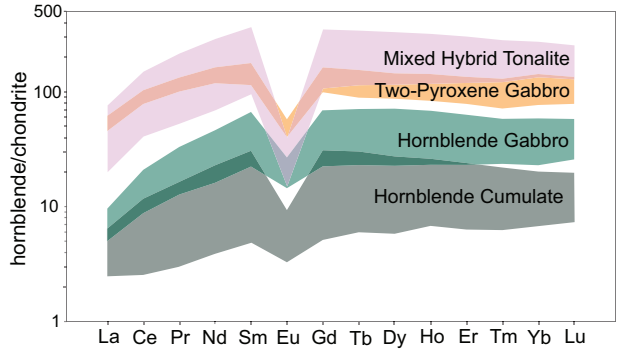

Fig. 11. Trace element patterns in hornblende from hornblende cumulate (sample 46), hornblende gabbro (samples 41 and 73), two-pyroxene gabbro (sample 22), and mixed hybrid tonalite (sample 23). Hornblende within the two-pyroxene gabbro (22) and mixed hybrid tonalite (23) occurs as a minimal (<5%) and interstitial phase that would have crystallized very late. Prior crystal fractionation (i.e. pyroxene for the two-pyroxene gabbro) likely controlled the resultant REE patterns that the late-stage hornblende took on in sample 22 and 23. Strong negative Eu anomalies indicate that hornblende must have begun crystallizing well after plagioclase. Trace element concentrations were measured in hornblende by LA-ICP-MS (Supplementary Data Electronic Appendix 2).

clinopyroxene likely controlled the resultant REE pattern that the late-stage (replacive) hornblende took on. The low modal abundance (<5%) and crystal shape (anhedral, interstitial) of the hornblende within the two-pyroxene gabbro unit also indicates it was one of the last minerals to crystallize.

Choosing a model starting composition

Mafic samples are too poor in Mg to be considered primitive magmas [they have MgO <6 wt % and Mg# <60, where Mg# is 100Mg/(Mg + Fe^T); see Baker *et al.*, 1994]. Relatively low Ni (<56 ppm) and Cr (<116 ppm) in all samples indicate that the most mafic magmas had significant fractionation of pyroxene and olivine before emplacement at the exposed crustal level. As Annen *et al.* (2006) pointed out, differentiation of mantle-derived basalt is likely at deep crustal levels near the Moho (in deep crustal hot zones), and this may be the reason for the lack of primitive basalts at shallow crustal levels. Hence, our starting point was chosen based on the most primitive samples in the suite, which could be representative of a parental magma to the system. The most primitive sample in this suite that unequivocally represents a liquid is a basaltic andesite (sample 38A) with 55·6 wt % SiO_2 and 4·1 wt % MgO, Mg# 39, 6 ppm Ni, and relatively low REE abundances. Other samples with more mafic compositions (<53 wt % SiO_2) cannot reliably be considered as liquid representatives because of high phenocryst abundances within the volcanic rocks (i.e. plagioclase-phyric rocks), or because of cumulate textures within the plutonic rocks (especially hornblende). Another subset of basaltic andesites are just as primitive as sample 38A, but are higher in Fe and Ti, and show tholeiitic affinities (Figs 5a and 6a, c) (e.g. sample 106). Given their elevated REE abundances and other distinctive chemical characteristics (Figs 7 and 8), they cannot be parental to the rest of the sample suite.

H_2O contents

Magmatic H_2O contents were estimated for both plutonic rocks (hornblende gabbro, two-pyroxene gabbro, and tonalite) and volcanic rocks (dacite lava and a plagioclase-phyric basaltic andesite hypabyssal intrusion). Estimates were made with the hygrometer of Waters & Lange (2015) using plagioclase mineral chemistry, whole-rock major element chemistry, and assumed temperatures and pressures. Pressures used are 2·5 kbar, and represent the deepest level of exposure.

The following temperatures were used for hygrometer inputs: 850–950°C for felsic melts and 1100–1200°C for mafic melts. Although mafic in composition, hornblende gabbro samples had lower temperature inputs (950–1000°C; Blatter *et al.*, 2013), since we assume that they coexisted with the more felsic liquids (discussed below).

Hygrometer results are as follows and are included in Supplementary Data Electronic Appendix 4 (Table S4). Basaltic-andesite samples (52–53 wt % SiO_2) yield H_2O contents of 1·3–4·7 wt %. Mafic plutonic rocks yield magmatic H_2O contents of 0·4–2·1 wt % for two-pyroxene gabbro, and 3·9–5·9 wt % for hornblende gabbro. H_2O contents ranging from 3·4 to 6·2 wt % were calculated for felsic plutonic and volcanic samples.

These H_2O estimates are similar to those of hydrous arc melts (Wallace, 2005; Plank *et al.*, 2013; Nandedkar *et al.*, 2014). Early fractionation of anhydrous ultramafic and mafic minerals (i.e. plagioclase, olivine, and pyroxenes) from a hydrous basaltic parental magma will increase the H_2O wt % of the resulting melts. Thus, basaltic andesites with magmatic H_2O contents of up to 6% can reasonably be produced by differentiation from basalts with <2 wt % H_2O (e.g. Gaetani *et al.*, 1993; Sisson & Grove 1993). The abundance of miarolitic cavities within hornblende-bearing enclaves of andesitic composition (Fig. 4b) also supports moderate water contents within intermediate melts for the larger-scale regional magmatic plumbing system.

Thermodynamic modeling via MELTS

We first modeled potential magma fractionation pathways using the thermodynamic software package rhyolite-MELTS version 1.2.0 (Gualda *et al.*, 2012) to test whether the chosen basaltic andesite starting liquid can reproduce more evolved compositions via fractional crystallization. Starting liquids were tested using rhyolite-MELTS (MELTS) with varying input parameters [2–6 kbar; oxygen fugacities (fO_2) buffered between FMQ − 1 and FMQ + 2, where FMQ is the fayalite–magnetite–quartz buffer, and 0·5–5·2 wt % H_2O]. Although MELTS is not recommended for modeling the evolution

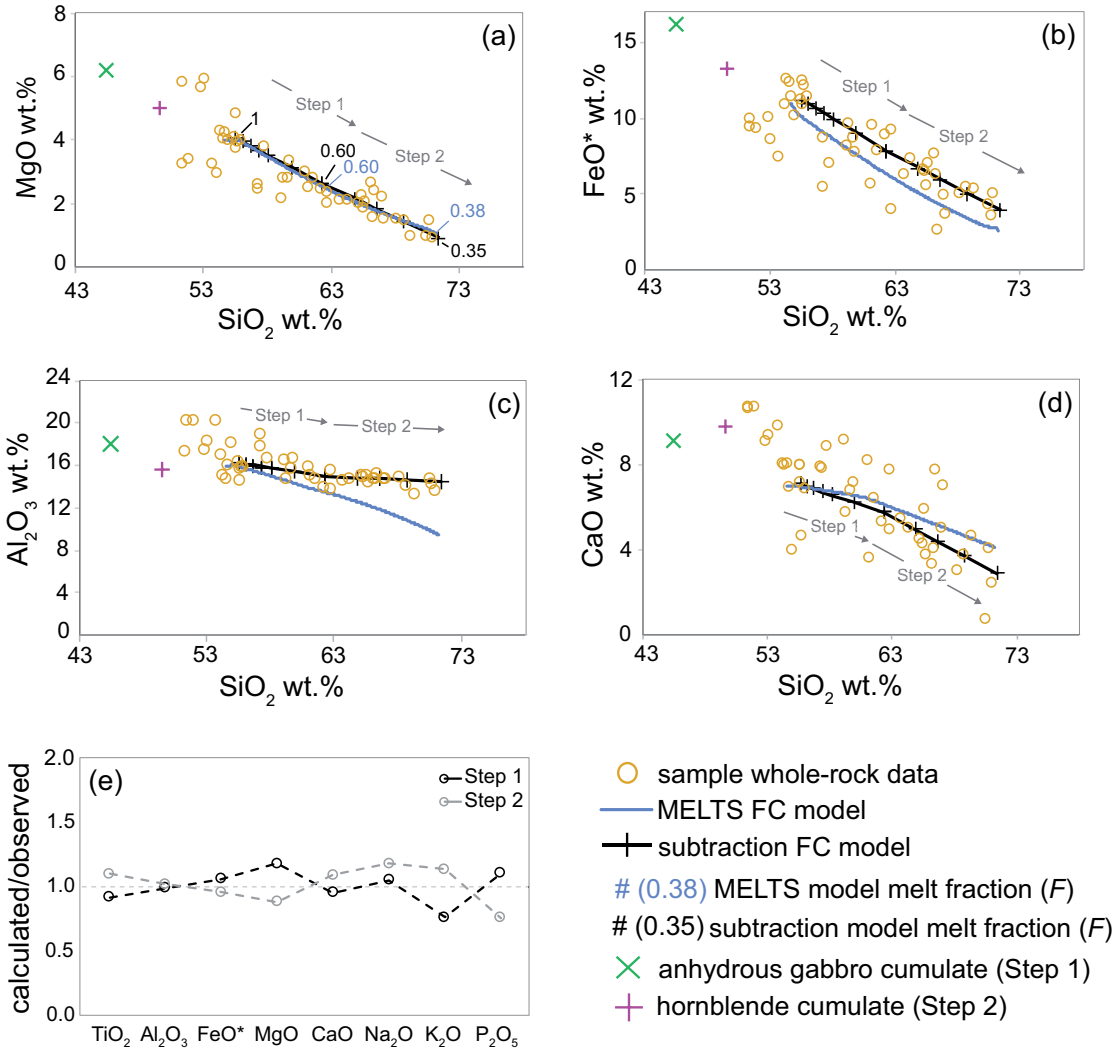

Fig. 12. (a–d) Thermodynamic modeling (MELTS) calculations in blue and simple subtraction fractional crystallization (FC) in black, compared to volatile-free (normalized) whole-rock data (yellow circles) for MgO, FeO*, Al_2O_3, and CaO vs SiO_2 wt %. FeO* indicates FeO_{total}. Compositions of mineral assemblages for simple subtraction FC are shown in green '×' symbol (anhydrous gabbro cumulate) and purple '+' symbol (hornblende cumulate). Two steps were conducted for simple subtraction FC. Step 1 models basaltic andesite to andesite (55·6–62·3 wt % SiO_2) ($F = 1$–0·6), with 40% fractionation of an anhydrous gabbroic assemblage. Step 2 models andesite to rhyolite (62·3–71·4 wt % SiO_2) ($F = 0·6$–0·35), with 25% further fractionation of a hydrous hornblende assemblage. Outputs from MELTS are provided in Supplementary Data Electronic Appendix 5. (e) Calculated versus observed compositions. Observed compositions are from the trendline of the whole-rock dataset in (a)–(d). Relative percent differences between the calculated vs observed compositions are <20%, with the exception of –24% difference for K_2O at the end of Step 1 ($F = 0·6$), and P_2O_5 at the end of Step 2 ($F = 0·35$) (modeling plots for K_2O and P_2O_5 not shown; see text for details).

of intermediate to felsic melts in calc-alkaline systems (Gualda *et al.*, 2012), our goal was to model fractional crystallization from mafic to intermediate compositions where hydrous phases are not expected.

MELTS effectively modeled closed-system fractional crystallization of the parental basaltic andesite magma (55·6 wt % SiO_2) to produce andesite (63 wt % SiO_2) after 40% fractionation (Fig. 12). Best-fit input parameters were 2·5 kbar pressure (isobaric), fO_2 of FMQ + 1, and initial H_2O of 1·5 wt %. The latter was considered a conservative estimate for mafic samples from hygrometer calculations. Inputs with higher and lower water contents produced non-ideal FeO_{total} and TiO_2 trends relative to SiO_2. Some examples of non-ideal trends are summarized in Supplementary Data Electronic Appendix 5 (Fig. S3).

The best-fit thermodynamic model has a liquidus at 1125°C, with magnetite as the first crystallizing phase (Supplementary Data Electronic Appendix 5, Table S5). At 1115°C and a melt fraction (F) of 0·99, plagioclase (An# 67) nucleates and fractionates alongside magnetite. Orthopyroxene fractionates early (1110°C, $F = 0·96$) in a melt with 55·8 wt % SiO_2, followed by clinopyroxene fractionating later (1064°C, $F = 0·68$) in a melt with

60·8 wt % SiO_2. By 1042°C, 40% of the melt has crystallized an assemblage of plagioclase, orthopyroxene, clinopyroxene, and magnetite, all of which are observed phases in Alisitos samples. The remaining melt fraction ($F = 0·60$) has a composition of 63 wt % SiO_2 and 2·4 wt % MgO, similar to the intermediate–felsic boundary for the sample suite (63 wt % SiO_2 and 2·2 wt % MgO) (Fig. 12a).

MELTS is not expected to provide reliable results for differentiating to more evolved samples, as it cannot model hornblende fractionation. We know that hornblende is an important crystallizing phase in the Alisitos arc because of the large meter-scale bodies of hornblende gabbro and centimeter-scale hornblende-bearing enclaves. We also know that it is a late crystallizing phase, both from textural relationships in plutonic rocks and from the strong negative Eu anomalies in hornblende minerals described above and shown in Fig. 11 (i.e. it begins crystallizing after plagioclase). Thus, when continuing MELTS modeling to 925°C, 62% of the melt has crystallized plagioclase, orthopyroxene, clinopyroxene, magnetite, and ilmenite (Supplementary Data Electronic Appendix 5, Table S5), but no hornblende. However, even without hornblende, the remaining melt fraction ($F = 0·38$) has a composition similar to the felsic members of the suite with ~71 wt % SiO_2, with model trends that match sample trends for some oxides but not others (e.g. CaO, Al_2O_3, and P_2O_5). CaO begins to level off early in the MELTS model, because plagioclase An# (67) is too low in CaO from its nucleation onwards (Fig. 12d). The model trend for Al_2O_3 is also too low compared to the samples, because MELTS over-fractionates plagioclase from 63 SiO_2 wt % onwards (Fig. 12c). The model trend for P_2O_5 (not shown) is too high from 63 SiO_2 wt % onwards, because MELTS does not fractionate apatite.

The slight inflection in the compositional trends at 63 wt % SiO_2 within the Alisitos rocks indicates a change in the fractionating assemblage, where amphibole fractionation has likely influenced the liquid line of descent between andesite and rhyolite compositions. Below, we test this hypothesis with our known mineral compositions from EMPA analyses by completing a non-thermodynamic, but compositionally constrained, simple subtraction model. In this model, we present the initial (Step 1) removal of a dominant two-pyroxene cumulate supported thermodynamically from MELTS, followed by a second (Step 2) removal of a hydrous amphibole cumulate that is supported in the field and petrographically.

Simple subtraction fractional crystallization

Simple subtraction modeling was used to test whether closed-system fractional crystallization of the selected parental magma can reproduce the observed suite of differentiated compositions. The benefit of this method is that the subtraction model uses known mineral compositions as fractionates, but uses MELTS as a guide for fractionating proportions. This fractionation model assumes mass balance, where the relationship between the concentration of an oxide in the parental magma (C_P), the fractionated mineral assemblage (C_A), and remaining melt (C_R) is

$$C_R = [C_P – (C_A X)]/[1 – X].$$

In this equation, C is the concentration (wt %) of the oxide of interest and X is the fraction of minerals removed from the parental magma. The fraction of melt remaining is defined by $[1 – X]$.

Several mineral assemblages were tested as potential fractionates that could drive differentiation. Mineral compositions were from EMPA analyses (Supplementary Data Electronic Appendix 2, Tables S1A–S1E), with the exception of an apatite composition from Sha & Chappell (1999). Mineral proportions were adjusted based on petrography and MELTS results until an optimal fit between the model and sample data was achieved.

Model results (Fig. 12) show that a two-step fractionation process can produce linear trends in oxides that mimic the observed oxide trends of the sample suite. Step 1 fractionates an anhydrous gabbro cumulate consisting of plagioclase (59%), orthopyroxene (24%), augite (4%), magnetite (10%), and ilmenite (3%) (Mineral Assemblage 1, Table 4). This assemblage is similar to that predicted by MELTS; however, it includes slightly higher amounts of orthopyroxene, clinopyroxene, and ilmenite, and lower amounts of magnetite. Fractionation Step 1 is best represented by two-pyroxene gabbro lithologies present (rarely) in the southern volcano-bounded basin. This step adequately models the major-element differentiation trend from basaltic andesite (55·6 wt % SiO_2) to andesite (62·3 wt % SiO_2) compositions, after 40% fractionation ($F = 0·6$).

Step 2 begins where Step 1 ends at $F = 0·6$, with evidence provided by the noticeable change in slope on the wt % Al_2O_3 Harker diagrams in Fig. 12c. In contrast to Step 1, the fractionating cumulate is amphibole-rich, consisting of magnesio-ferri-hornblende (39%), plagioclase (51%), magnetite (6%), ilmenite (3%), and apatite (1%) (Mineral Assemblage 2, Table 4). These phase proportions are a good match for hornblende-rich lithologies (hornblende gabbros, hornblende cumulates, and hornblende-bearing enclaves), where hornblende is more abundant in the differentiated plutonic rocks. This step adequately models the major element differentiation trend from andesite compositions (62·3 wt % SiO_2) to rhyolite compositions (71·4 wt % SiO_2) after 25% more fractionation ($F = 0·35$). A total of 65% fractionation to generate rhyolite compositions is similar to what fluid dynamical models suggest (between 50–70%) (Dufek & Bachmann, 2010; Deering *et al.*, 2011).

Although realistically we do not expect such a sharp transition from no hornblende crystallizing to 39% of the fractionating assemblage, the trends produced by simple subtraction modeling are remarkably similar to the sample trends (Fig. 12). The model exhibits linear

Table 4: Simple subtraction fractional crystallization modeling melt and cumulate compositions

	Step 1: Parental magma	Mineral assemblage 1	Component (spot):	Opx (22_2-3)	Cpx (25_3-2)	Plag (73_3-3)	Mag (70C_1L)	Ilm (70C_2D)	Melt fraction (*F*)				
	38A	anhydrous gabbro cumulate	%:	24%	4%	59%	10%	3%	1	0·9	0·8	0·7	0·6
SiO_2	55·57	45·43		53·44	51·14	51·80	0·10	0·03	55·57	56·70	58·10	59·91	62·32
TiO2	1·19	1·53		0·28	0·62	n.a	0·08	47·5	1·19	1·15	1·11	1·05	0·97
Al_2O_3	16·26	18·20		1·17	1·94	30·15	0·38	0·03	16·26	16·05	15·78	15·43	14·98
FeO*	11·18	16·20		19·87	11·98	0·59	91·41	49·70	11·18	10·62	9·92	9·02	7·81
MnO	0·21	0·21		0·51	0·52	n.a	0·12	1·70	0·21	0·21	0·21	0·21	0·21
MgO	4·06	6·22		23·6	13·6	n.a	0·06	0·07	4·06	3·82	3·52	3·14	2·62
CaO	7·09	9·11		1·55	19·8	13·5	n.a	n.a	7·09	6·87	6·58	6·22	5·74
Na_2O	3·84	2·27		0·00	0·23	3·83	n.a	n.a	3·84	4·01	4·23	4·51	4·89
K_2O	0·45	0·02		n.a	n.a	0·03	n.a	n.a	0·45	0·50	0·56	0·63	0·74
P_2O_5	0·14	0·00		n.a	n.a	n.a	n.a	n.a	0·14	0·16	0·18	0·20	0·23
Total	99·99	99·21		100·42	99·85	99·88	92·16	99·00	99·99	100·08	100·18	100·32	100·51

	Step 2: Starting melt	Mineral assemblage 2	Component (spot):	Hbld (41_1-1)	Plag (63_1-2)	Ilm (46_9)	Mag (46-08_3)	Ap (AB195ME[1])	Melt fraction (*F*)				
	Step 1, $F=0.6$	hornblende cumulate	%:	39%	51%	3%	6%	1%	0.6	0.5	0.45	0.4	0.35
SiO_2	62·32	49·60		51·70	57·65	0·02	0·10	n.a	62·32	64·87	66·57	68·69	71·43
TiO2	0·97	1·52		0·23	n.a	47·7	0·00	n.a	0·97	0·86	0·78	0·69	0·57
Al_2O_3	14·98	15·70		4·94	26·95	0·02	0·38	n.a	14·98	14·83	14·74	14·62	14·46
FeO*	7·81	13·30		16·56	0·26	43·00	90·90	n.a	7·81	6·71	5·97	5·05	3·87
MnO	0·21	0·35		0·27	n.a	8·01	0·09	n.a	0·21	0·18	0·17	0·14	0·11
MgO	2·62	5·00		12·8	n.a	0·05	0·03	n.a	2·62	2·15	1·83	1·43	0·93
CaO	5·74	9·78		12·1	8·86	n.a	n.a	54·3	5·74	4·94	4·40	3·72	2·86
Na_2O	4·89	3·53		0·64	6·44	n.a	n.a	n.a	4·89	5·16	5·34	5·56	5·85
K_2O	0·74	0·20		0·17	0·27	n.a	n.a	n.a	0·74	0·84	0·91	1·00	1·12
P_2O_5	0·23	0·42		n.a	n.a	n.a	n.a	41·7	0·23	0·20	0·17	0·14	0·10
Total	100·51	99·43		99·41	100·43	98·75	91·50	96·00	100·51	100·74	100·88	101·06	101·30

FeO* is total FeO. n.a., not analyzed.
[1]Apatite composition from sample AB195ME (mafic enclave), Sha & Chappell (1999).

decreasing trends for MgO and FeO_{total}, which are continuous from Step 1 to Step 2, but do not perfectly mimic the slight inflection in MgO at ~63 wt % SiO_2 (Fig. 6d). Decreasing trends are accurately modeled for CaO and Al_2O_3, as well as TiO_2 (not shown), including the slight inflections ~ 63 wt% SiO_2. For P_2O_5, the inflection from increasing to decreasing sample trends ~ 63 wt% SiO_2 is accurately modeled due to the minor (1%) fractionation of apatite occurring in Step 2. Model trends for wt % MnO, K_2O, and Na_2O (not shown) generally match observed sample trends.

We evaluate the validity of the model by comparing the composition of the calculated melt at $F = 0{\cdot}6$ (end of Step 1) to the average composition of observed samples with the same wt % SiO_2, and expressing the result as a ratio (Fig. 12e). A perfect fit would have a ratio of 1. The same is done for the end of Step 2 at $F = 0{\cdot}35$. Calculated melt fractions show a good fit to all observed samples, where relative percent differences between calculated versus observed are <20% (ratio value of 0·2). Exceptions include K_2O and P_2O_5 (not shown), which are in such low quantities (<1 wt %) that slight variations between observed and calculated concentrations result in a higher relative percent difference. For example, comparing P_2O_5 quantities of 0·10 wt % (calculated) vs 0·13 wt % (observed) at $F = 0{\cdot}35$ results in a –24% difference.

Trace element modeling

Modeling of trace element variation by crystal fractionation uses the same phase assemblage and crystallizing proportions as in the simple subtraction modeling. We employ the Rayleigh fractionation equation (Gast, 1968). Values of K_d used for trace element modeling are from the literature (see Fig. 13).

Trace element trends and total abundances for many of the mafic to intermediate samples can be effectively modeled as results of up to 40% fractionation ($F = 0{\cdot}6$) of the basaltic andesite parental melt via fractionation of the Step 1 mineral assemblage described above (anhydrous gabbro cumulate, Table 4) (Fig. 13a). However, this is not true for the more felsic samples (>63 wt % SiO_2). Total abundances modeled well for the MREE and HREE (up to 62·8 wt % SiO_2), but the match is not as good for the LREE (Fig. 13a). The model is highly dependent on choice of parental magma. Because we are using whole-rocks as a representation of liquid composition, any small excess in REE-bearing minerals in the rock (including pyroxene) can distort the resulting REE pattern.

REE patterns for dacitic to rhyolitic compositions do not show continued positive correlation in abundance with SiO_2 as they do for the mafic to intermediate rocks. They instead show nearly complete overlap with the modeled $F = 1$ to $F = 0{\cdot}6$ results (Fig. 13b). Thus, the fractionating assemblage in Step 2 (hornblende cumulate; Table 4) needs to produce a decrease in REE abundances to be successful, but not in any regular way with increasing SiO_2.

Decreasing REE trends can be produced if the appropriate K_d values for REE in amphibole are chosen (as

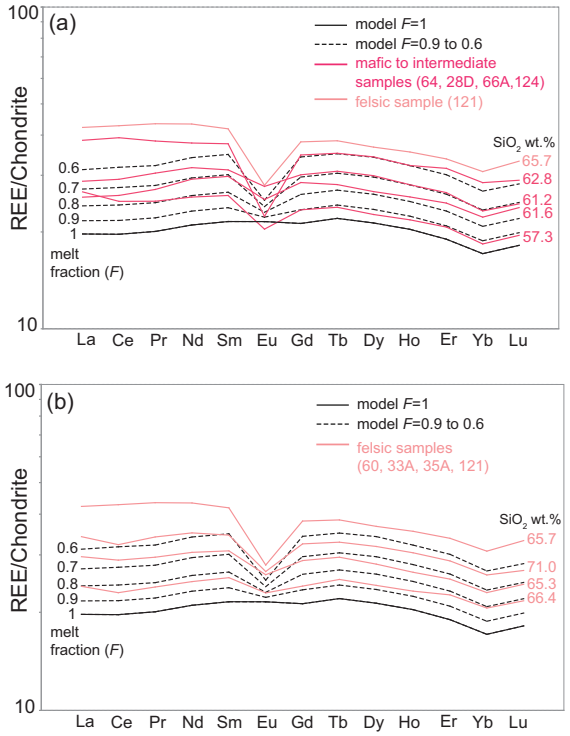

Fig. 13. (a) REE model results (dashed lines) for Step 1 using gabbro fractionation to drive basaltic andesite ($F = 1$) to andesite ($F = 0{\cdot}6$). Gabbro cumulate mineral proportions are identical to major element simple subtraction modeling proportions. Fractionation of an anhydrous gabbro cumulate produces similar MREE and HREE abundances to andesites (red lines) up to 62·8 wt % SiO_2. (b) REE abundances for dacitic to rhyolitic compositions show nearly complete overlap with modeled $F = 1$ to $F = 0{\cdot}6$ results (where REE abundances appear to have no simple relationship to SiO_2 content). Thus, simple fractionation modeling cannot match REE patterns for samples that have >63 wt % SiO_2. K_d values for plagioclase, orthopyroxene, augite, magnetite, and ilmenite are from published values (Paster *et al.*, 1974; Arth, 1976; Fujimaki *et al.*, 1984; Lemarchand *et al.*, 1987).

amphibole is 39% of the fractionating assemblage). There are a range of possible K_d values to choose from, both from the literature and from K_d values calculated in this study (K_d = measured trace elements in amphibole/whole-rock). Depending on the choice, resulting bulk D values for the REE can be greater than or less than 1, which will produce either decreasing or increasing REE abundances with increasing SiO_2, respectively (see Supplementary Data Electronic Appendix 6, Fig. S4 for further discussion and model presentations).

Ultimately, the trace element modeling from $F = 0{\cdot}6$ to $F = 0{\cdot}35$ is not constrainable because of the non-linear variation of REE abundances with increasing SiO_2. The modeling is further limited by the fact that we are using whole-rock compositions as a proxy for liquid compositions. Identifying representative liquid compositions in intermediate to felsic plutonic rocks is particularly difficult, where silicic cumulates are commonly geochemically cryptic (Gelman *et al.*, 2014). In addition, trace phases in whole-rock, such as monazite, zircon, apatite, and titanite, can profoundly affect REE patterns, and these minerals are more common in felsic rocks. Localized

growth of these minerals, even in minute quantities, may cause significant variations in REE patterns that would not be representative of the crystallizing liquids. Intermediate to felsic plutonic rocks show evidence of minor (<1%) amounts of titanite, zircon, and apatite.

Implications of modeling results

Closed-system processes, dominated by fractionation of anhydrous mineral assemblages, clearly can be responsible for driving differentiation from basaltic andesite to andesite. Evidence comes from both the limited isotopic range of the samples, as well as field evidence for the existence of similar anhydrous gabbroic assemblages within some of the deeper levels of the plutonic exposures. The level within the crust where this first fractionation step dominantly occurs is unconstrained by this study, but must be deeper than the current level of exposure, given the limited outcrop abundance of these fractionates. Figure 14 is a simple schematic diagram illustrating how we interpret the fractionation steps within the Alisitos arc crustal section. Simple crystal fractionation is a common hypothesis for producing evolved melts in many oceanic arc systems (e.g. Haraguchi *et al.*, 2003; Greene *et al.*, 2006; Straub, 2008; Jagoutz, 2010; Garrison *et al.*, 2012). Modeling from some of these studies indicates that the evolved melts can be generated from an early removal of either anhydrous gabbroic fractionates (Greene *et al.*, 2006) or hydrous amphibole fractionates (Jagoutz, 2010; Garrison *et al.*, 2012), with the difference likely being related to initial magmatic H_2O contents and the bulk composition of the melt (Sisson & Grove, 1993).

For the next differentiation step, from andesite to rhyolite, major element compositions can be successfully modeled by continued simple fractional crystallization at the level of exposure of the pluton (Fig. 14). Clearly, the fractionation of amphibole in this step is important, as evidenced by the high proportion of hornblende in the more evolved plutonic rocks, and its presence in hornblende-rich lithologies (hornblende gabbros, hornblende cumulates, and hornblende-bearing enclaves). Slight inflections ~63 wt % SiO_2 in both major and trace element trends support a more important role for amphibole fractionation. This is probably a result of both decreasing temperature and increased water contents driven by previous fractionation of anhydrous assemblages. However, this step is more difficult to model for trace elements, as described above, and potentially may involve more complex open-system processes.

If open-system processes involving pre-existing crust are active in the evolution of rhyolitic liquids, these must be limited to incorporation of material that is not isotopically distinct. Hence, that incorporated material cannot be very old and would probably include remelting or assimilation of relatively recent and geochemically similar plutonic roots. This process cannot be effectively modeled or constrained given the erratic control of trace minerals described above, and the difficulty of choosing an assimilant.

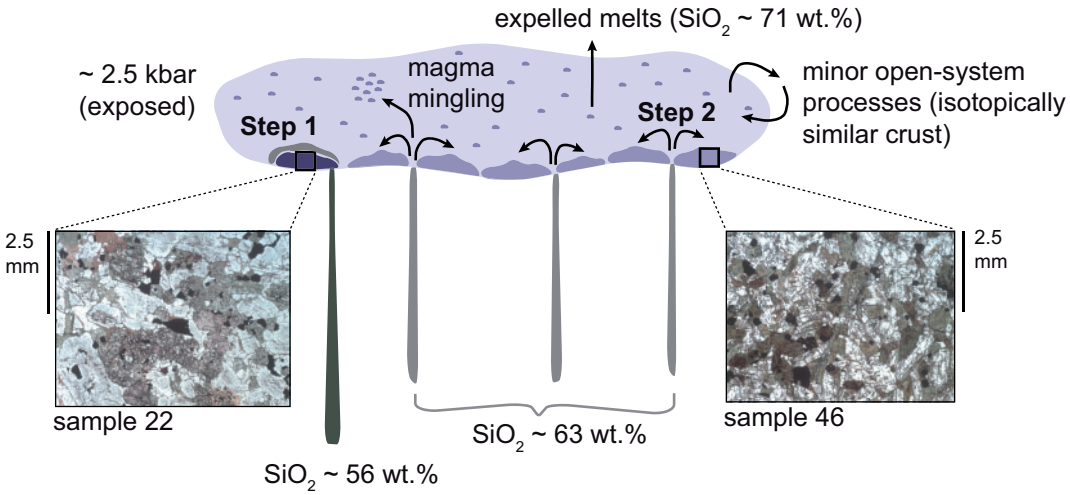

Fig. 14. A simple schematic diagram illustrating our interpretation of the dominant petrologic processes driving differentiation within the exposed mid to upper crustal units of the Rosario segment, Alisitos arc. Differentiation occurs in a two-step process: Step 1 drives basaltic andesite to andesite melt compositions through the fractionation of an anhydrous gabbroic assemblage (dominantly occurs at depth); Step 2 drives andesite to rhyolite melt compositions through the fractionation of an amphibole-rich assemblage (*in situ*).

Back-mixing between the most differentiated magmas and intermediate magmas may also play a role in developing arc crust. The observation of two potential trends in the Yb and Zr versus SiO_2 plot (a higher trend and a lower trend in Fig. 7d and g) provide a clue. Lee & Bachmann (2014) described similar trends produced from MELTS modeling, where the higher trend represents crystal fractionation, and the lower trend represents mixing between a highly differentiated (Zr-saturated) rhyolite and an intermediate andesite (Zr-undersaturated). Field exposures of mingled magmas (Fig. 4a) support this hypothesis.

Crustal evolution model

The following is a proposed crustal evolution model for the Rosario segment of the Alisitos arc, and is developed using the previously described field, petrological, and geochemical relationships. The entire upper volcanic to middle plutonic crustal column, from basaltic andesite to rhyolite compositions, was produced within ~8 Myr (113·9–106·4 Ma). Units were all derived from a uniform mantle source with initial ε_{Nd} of ~6·6. Low Sr/Y and Ce/Y ratios suggest a thin arc crust and Moho depths were likely <20 km (Fig. 10; Mantle & Collins, 2008; Chapman *et al.*, 2015). These are medium- to low-K compositions, and there is no evidence for any contribution from older cratonic continental crust.

Crustal growth processes were predominantly closed-system, where fractional crystallization produced the range of mafic to intermediate compositions preserved in both the plutonic and volcanic rocks. Differentiation from basaltic andesite to andesite compositions, with no concomitant change in isotopic character, most likely occurred via fractionation of anhydrous gabbroic assemblages at a depth beneath the level of exposure, given the limited abundance of that type of lithology in the plutonic outcrops. However, continued fractionation to more felsic compositions (rhyolite) via fractionation of amphibole-bearing assemblages probably occurred at the level of exposure (~2·5 kbar), given the abundance of hornblende-rich lithologies in the plutons. Back-mixing between all magma types is permissible.

Volcanic rocks formed a 3–5 km thick section of erupted rocks and hypabyssal intrusions that were fed from underlying plutonic reservoirs. The system can be visualized as one where magmas rose to shallow crustal levels through dikes and sills, were erupted, and then older, basal layers were engulfed by growing plutons. The compositional ranges of both the volcanic and plutonic rocks are nearly identical. The only variation appears to be that some lavas and sills have tholeiitic compositions, while the plutons do not, suggesting that drier magmas occasionally rose directly to surface or near-surface levels. A younger age from a tholeiitic sill suggests that these drier magmas may have been erupting and intruding during the late stages of arc rifting, perhaps as a result of increased rates of extension as proposed on the basis of geologic relations by Busby *et al.* (2006).

Comparison to a modern analog: Izu–Bonin arc

The Cretaceous Alisitos arc was first described as an on-land analog to the active Izu–Bonin arc by Fackler-Adams & Busby (1998) and Busby *et al.* (2006). Based on stratigraphic and structural arguments, these authors described the Alisitos as an arc that was undergoing extension and eventual rifting, similar to the extension and rifting phase of the Izu–Bonin arc. The geochemistry presented here provides a strong corroboration to that comparison—the Alisitos is a low- to medium-K arc system, with relatively flat REE patterns and low Sr/Y. However, the Izu–Bonin arc has been shown to have significant across-arc geochemical variability from the arc front, the active rift located immediately behind the arc front, and the rear arc (Fig. 15a) (e.g. Hochstaedter *et al.*, 2001; Ishizuka *et al.*, 2006; Tollstrup *et al.*, 2010). These studies showed that geochemical variations across the arc (shown as shaded regions in Fig. 15b–d) encompass a progressive enrichment from a fluid-rich, but LREE-depleted arc front to a LREE-enriched rear arc. The active rift in between has flat REE patterns.

Comparison of the southern Alisitos arc (Rosario segment) with the modern Izu–Bonin arc shows a remarkable similarity to Izu's active rift segment (Figs 15 and 16). This includes similar LILE enrichments (except for Ba), HFSE depletions (not shown), and flat REE patterns (Fig. 15c). The flat REE patterns of the Rosario segment and active rift samples translate into similar $[La/Yb]_N$ ratios of ~1–1·5, which contrasts with lower ratios in the arc front (<1), and higher ratios in the rear arc (generally >1·5) (Fig. 16a).

Other trace element ratios (Nb/Ta vs Zr/Nb, Nb/Yb vs SiO_2, La/Sm vs Nb/Zr) have also been shown to clearly distinguish between the Izu–Bonin arc front, active rift, and rear arc (Hochstaedter *et al.*, 2001; Clift *et al.*, 2005). The Rosario segment samples are most similar to active rift ratios, and have limited variation (Figs 16a–d). La/Sm vs Nb/Zr displays depleted, non-continental-like values for both the Rosario segment and Izu–Bonin samples (Fig. 16d) (Clift *et al.*, 2005). These geochemical comparisons support prior interpretations (based on stratigraphic relationships) that the Rosario segment of the Alisitos arc was extending and beginning to rift (Busby *et al.*, 2006). There is not enough known about the geochemistry of other segments of the Alisitos arc to determine whether an arc front-like region exists elsewhere in this large terrane (Fig. 1a).

Rosario segment—insights at depth?

The Rosario segment of the Alisitos arc may represent an analog to the middle to upper crustal levels of the Izu–Bonin arc, including the intriguing low-velocity ($V_p = 6.0$–6.5 km s^{-1}) middle crustal layer (Suyehiro *et al.*, 1996; Tatsumi & Stern, 2006; Kodaira *et al.*, 2007;

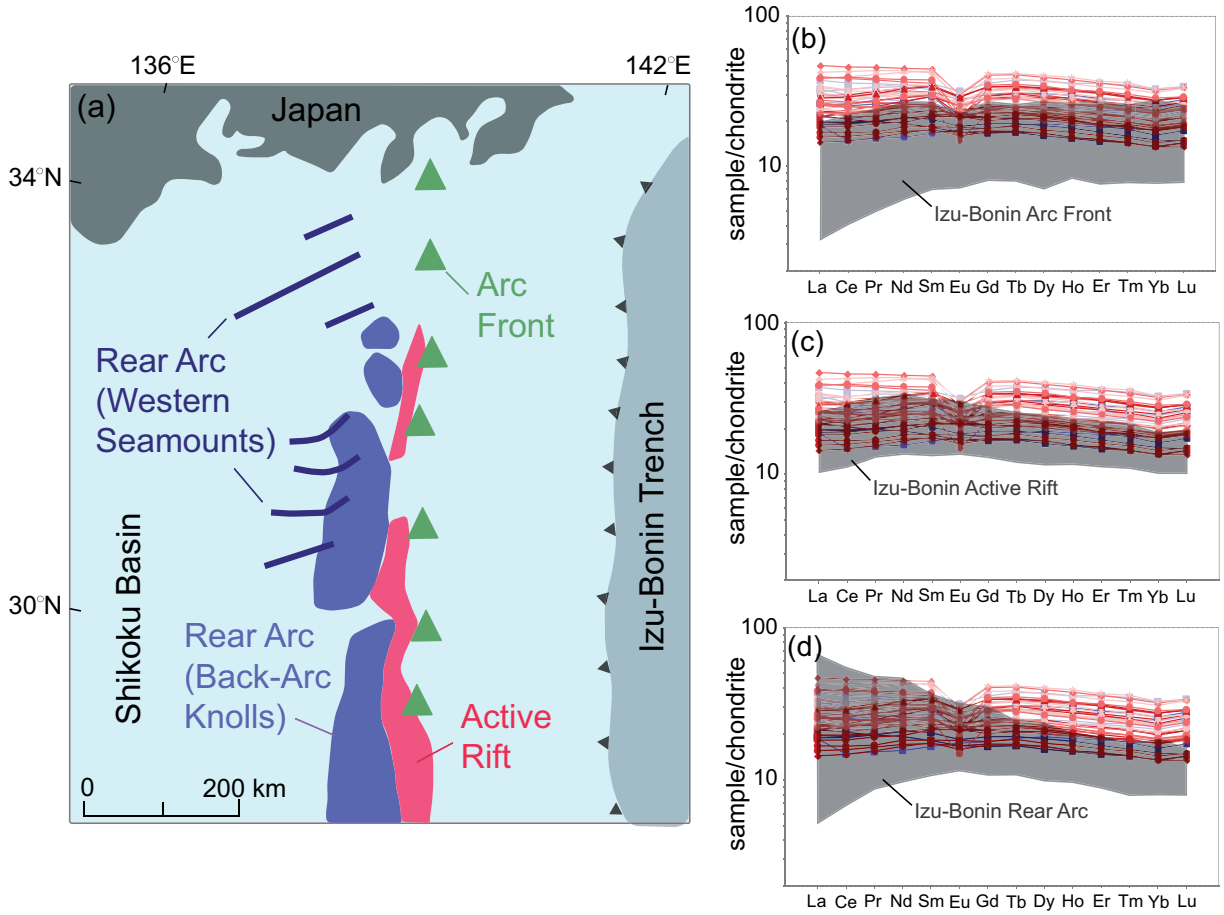

Fig. 15. Chondrite-normalized REE diagrams comparing across-arc segments of the Izu–Bonin arc to the southern volcano-bounded basin sample suite. Izu–Bonin across-arc regions for geochemical comparison are based on recent work by Heywood (2018), which reclassified the Izu–Bonin rear arc to include both back-arc knoll and western seamount samples, due to their geochemical similarities. (a) Map showing across-arc segments of the Izu–Bonin arc, from Ishizuka *et al.* (2006). Sample REE patterns are compared with Izu–Bonin arc front (b), active rift (c), and rear arc (d). Samples display REE abundances and flat REE patterns similar to the active rift samples (c). Sample legend as in Fig. 8.

Takahashi *et al.*, 2007) (Fig. 17). The transition from the erupted volcanics to plutonic root occurs at roughly similar depths (~5 km) to the transition to the 6·0–6·5 km s^{-1} V_p layer in the Izu–Bonin arc (Fig. 17). Based on exposure area, the most abundant plutonic lithology within the Rosario segment is tonalite, with an average composition of 66·5 wt % SiO_2 and 1·9 wt % MgO. The mid crustal plutons are likely derived from influx of previously differentiated magmas (broadly andesitic) formed by fractionating anhydrous assemblages in the deeper crust. Felsic melt generation is likely controlled by fractional crystallization of more hydrous assemblages *in situ*, and may include input from a small percentage of crustal melts or assimilants. This compares well with the model proposed by Annen *et al.* (2006) for the generation of intermediate and silicic igneous rocks in arcs. Interestingly, if hydrous parental melts are feeding the arc, both anhydrous and hydrous assemblages can drive differentiation at different stages. The fractionation of an early-stage anhydrous assemblage (i.e. gabbroic cumulate) will increase the H_2O wt % of the differentiated melt, and likely force the fractionation of a later-stage hydrous assemblage (i.e. amphibole-bearing cumulate) to form dacitic to rhyolitic residual melt.

Our study has addressed an important question about the timing of development of arc mid crust relative to upper crust. If the mid crust was developed early in the arc's history, and hence unrelated to the upper crust, then volcanic feeders would cross-cut the mid crust. If instead it developed in concert with the upper crust, the mid crust would grow and cannibalize the upper crust with time. Our mapping shows the latter; feeders for volcanic rocks (i.e. dikes and hypabyssal intrusions) do not cross-cut the plutons, but instead invade the lower levels of the upper crustal section (Fig. 3). Our geochemical studies support this interpretation; the mid crust and upper crust are genetically related. The tempo of arc crust growth was relatively rapid; the entire crustal section was built in less than 8 Myr.

CONCLUSIONS

The plutonic and volcanic rocks of the Rosario segment of the Cretaceous Alisitos oceanic arc provide an

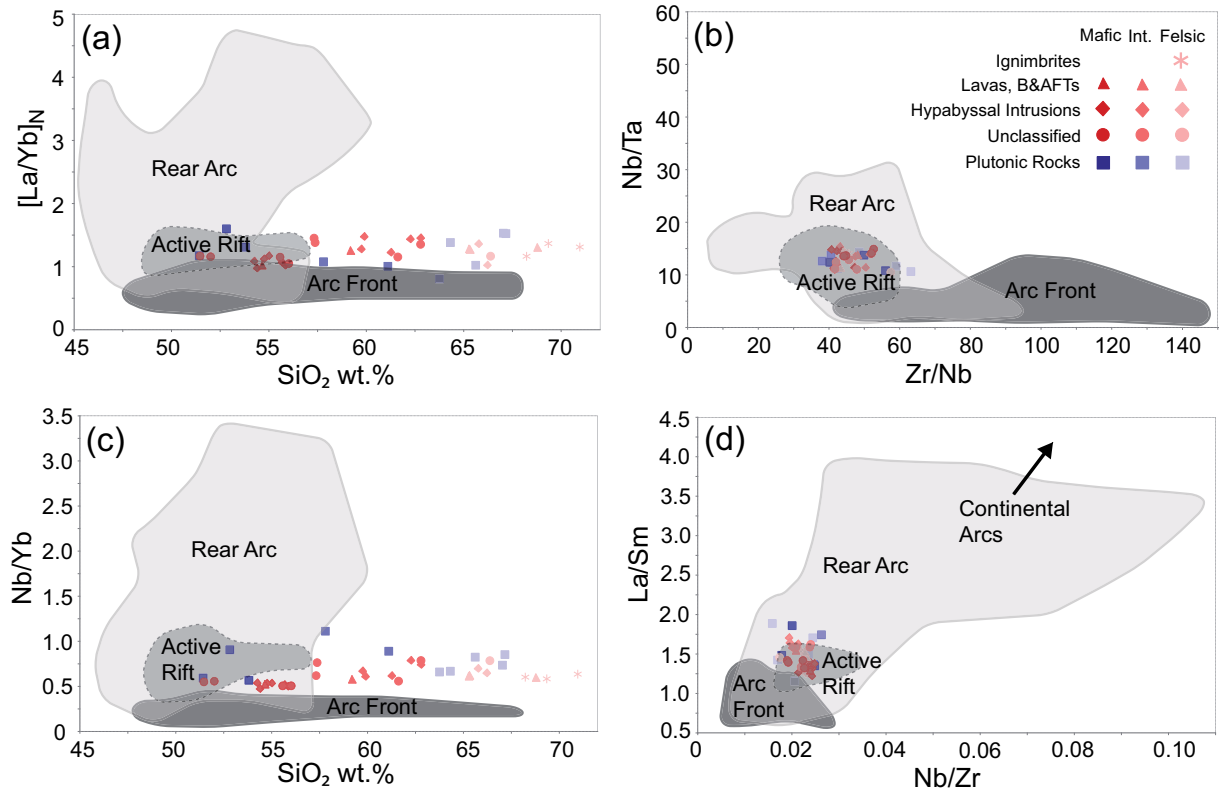

Fig. 16. Trace element bivariate and ratio plots that highlight samples of the southern volcano-bounded basin (Rosario segment, Alisitos arc) compared to Izu–Bonin arc segments. (a) Samples display similar $[La/Yb]_N$ ratios (~1–1·5) to the active rift, as a result of their flat REE patterns (see Fig. 15c). (b) Samples show similar Nb/Ta vs Zr/Nb values to the active rift. (c) Samples display limited trace element ratio (Nb/Yb) variation, similar to the active rift. (d) Both the Izu–Bonin arc and the southern volcano-bounded basin samples show depleted, non-continental-like La/Sm and Nb/Zr values (Clift *et al.*, 2005).

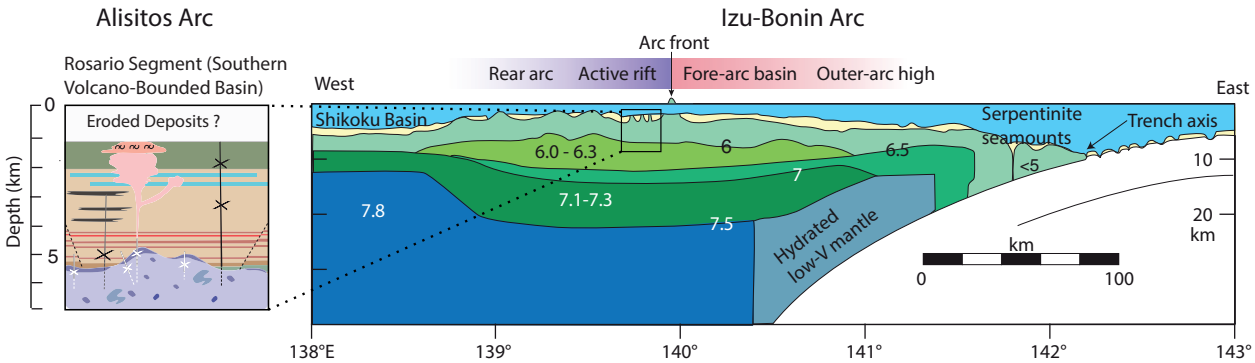

Fig. 17. We interpret the exposed plutonic rocks of the Rosario segment (southern volcano-bounded basin) as a field analog to the low-velocity ($V_p = 6·0–6·5\ km\ s^{-1}$) zone imaged in the Izu–Bonin arc (Suyehiro *et al.*, 1996; Busby *et al.*, 2017). The transition from erupted volcanics to the plutonic root occurs at roughly similar depths (~5 km) to the transition to the 6·0–6·5 km s^{-1} V_p layer in the Izu–Bonin arc. Geochemical data from the southern volcano-bounded basin are similar to the active rift of the Izu–Bonin arc (see Figs 15 and 16).

outstanding window into the petrologic processes involved in the generation and evolution of juvenile extensional oceanic arc crust. We have demonstrated that the plutonic and volcanic rocks are genetically linked, both physically and geochemically. Magmas rose to shallow crustal levels through dikes and sills, were partially erupted, and basal volcanic rocks were engulfed by growing plutonic phases. The intrusive contacts between plutonic rocks and volcanic rocks occur over a short vertical transition (<150 m), where stoped volcanic blocks and xenoliths of country rocks are common. The plutonic and volcanic units show compositional overlap for both major and trace element chemistry, and display similar evolutionary trends. Magma mingling is evident throughout the plutonic rocks, indicating continuous injection of mafic magmas into more

felsic reservoirs, and/or potential back-mixing between felsic and intermediate magmas.

Volcanic and plutonic rocks are predominantly low-K with flat REE patterns, and show LILE enrichment and HFSE depletion. Initial Nd and Pb isotope ratios overlap for all units and do not correlate with SiO_2 or other incompatible elements. They therefore provide evidence for the lack of involvement of old cratonic continental involvement. The limited range in initial ε_{Nd} values indicates that any incorporated crustal components must be isotopically similar to the host magma. This, together with low Sr/Y (<20) and Ce/Y (<0·6) ratios, is typical of a thin, immature oceanic arc crust with depleted signatures, like those of extensional western Pacific arcs.

Closed-system fractional crystallization was the main driver of differentiation from mafic to intermediate compositions within the arc. Fractional crystallization of a basaltic andesite is shown to produce the range of mafic to intermediate compositions preserved in both plutonic and volcanic rocks. Intermediate compositions (~63 wt % SiO_2) can be produced by 40% fractionation of an anhydrous gabbroic cumulate. The dominant location for this step of fractionation is inferred to be at deeper crustal levels, given the paucity (but not complete absence) of the inferred fractionating phases at the current crustal level.

The fractionating assemblage after 40% crystallization is inferred to change to a hydrous amphibole-bearing cumulate to produce the more felsic dacites and rhyolites present within the arc (up to a total of 65% crystallization). This amount of fractionation required is similar to what fluid dynamical models suggest (between 50–70%; Dufek & Bachmann, 2010; Deering *et al.*, 2011). These amphibole-bearing assemblages are widely exposed at the current crustal level; therefore this step is inferred to occur *in situ*.

We present a crustal evolution model for the Rosario segment of the Alisitos arc. During the generation of the short-lived arc crust (<8 Myr), basaltic andesite to rhyolite compositions were produced from a hydrous subduction-modified mantle source with no contributions from old cratonic continental crust. Differentiation from mafic to intermediate melt compositions likely occurred at depth (not exposed) through relatively closed-system processes, and more evolved magmas were produced within the magma reservoirs represented by the plutons at the current level of exposure.

Geochemical characteristics indicate the Rosario segment compares well with the active rift segment of the Izu–Bonin arc. Both display similar flat REE patterns and distinct trace element ratios. This suggests that our crustal section provides 3-D exposures into an active extensional arc. The lithological variation with depth within the Rosario segment matches well with the lithological variation inferred from the Izu–Bonin arc seismic profile. Therefore, the volcanic to plutonic transition may represent a good field analog for the transition to the $V_p = 6{\cdot}0$–$6{\cdot}5\ km\ s^{-1}$ middle crust imaged within the Izu–Bonin arc. Petrologic processes constrained within the exposed Rosario segment can thus be used to predict middle to upper crustal generation processes within active extensional arcs.

ACKNOWLEDGEMENTS

We thank Georg Zellmer, Olivier Bachmann, Ian Smith, Karsten Haase, and one anonymous reviewer for their insightful and constructive comments that helped improve the quality of this paper. A heartfelt thanks to Luan Heywood for providing companionship and discussions throughout the project. Our extensive dataset could not have been obtained without the generous field assistance from Simon Wing. Analytical work for this study was made possible with the assistance of Bruce Nelson and Scott Kuehner (both at University of Washington), and William Matthews (University of Calgary).

FUNDING

Funding for this project was provided by the National Science Foundation Grant NSF EAR 1347794. Additional support from the Geological Society of America, Western Washington University Geology Department, and Western Washington University Office of Research and Sponsored Programs (Arlan Norman Award Scholarship) was greatly appreciated. We further thank the Office of Research and Sponsored Programs (Western Washington University) for providing the generous funds required for an open access license to this paper.

SUPPLEMENTARY DATA

Supplementary data are available at *Journal of Petrology* online.

REFERENCES

Annen, C., Blundy, J. D. & Sparks, R. S. J. (2006). The genesis of intermediate and silicic magmas in deep crustal hot zones. *Journal of Petrology* **47**, 505–539.

Arth, J. G. (1976). Behaviour of trace elements during magmatic processes—a summary of theoretical models and their applications. *Journal of Research of the US Geological Survey* **4**, 41–47.

Bachmann, O. & Bergantz, G. W. (2004). On the origin of crystal-poor rhyolites: extracted from batholithic crystal mushes. *Journal of Petrology* **45**, 1565–1582.

Bachmann, O. & Huber, C. (2016). Silicic magma reservoirs in the Earth's crust. *American Mineralogist* **101**, 2377–2404.

Baker, M. B., Grove, T. L. & Price, R. (1994). Primitive basalts and andesites from the Mt. Shasta region, N. California: products of varying melt fraction and water content. *Contributions to Mineralogy and Petrology* **188**, 111–129.

Bickle, M., Arculus, R., Barrett, P., DeConto, R., Camoin, G., Edwards, K., Fisher, A., Inagaki, F., Kodaira, S., Ohkouchi, N., Pälike, H., Ravelo, C., Saffer, D. & Teagle, D. (2013).

Illuminating Earth s Past, Present, and Future, The International Ocean Discovery Program Science Plan for 2013–2023. https://www.iodp.org/about-iodp/iodp-science-plan-2013-2023

Blatter, D. L., Sisson, T. W. & Hankins, W. B. (2013). Crystallization of oxidized, moderately hydrous arc basalt at mid- to lower-crustal pressures: implications for andesite genesis. *Contributions to Mineralogy and Petrology* **166**, 861–886.

Brach-Papa, C., Van Bocxstaele, M., Ponzervera, E. & Quetel, C. R. (2009). Fit for purpose validated method for the determination of the strontium isotopic signature in mineral water samples by multi-collector inductively coupled plasma mass spectrometry. *Spectrochimica Acta Part B: Atomic Spectroscopy* **64**, 299–234.

Busby, C. (2004). Continental growth at convergent margins facing large ocean basins: a case study from Mesozoic convergent-margin basins of Baja California, Mexico. *Tectonophysics* **392**, 241–277.

Busby, C., Smith, D., Morris, W. & Fackler-Adams, B. (1998). Evolutionary model for convergent margins facing large ocean basins: Mesozoic Baja California, Mexico. *Geology* **26**, 227–230.

Busby, C., Fackler-Adams, B., Mattinson, J. & Deoreo, S. (2006). View of an intact oceanic arc, from surficial to mesozonal levels: Cretaceous Alisitos Arc, Baja California. *Journal of Volcanology and Geothermal Research* **149**, 1–46.

Busby, C. J., Tamura, Y., Blum, P., et al. (2017). The missing half of the subduction factory: shipboard results from the Izu rear arc, IODP Expedition 350. *International Geology Review* **59**, 1677–1708.

Busby-Spera, C. J. & Boles, J. R. (1986). Sedimentation and subsidence styles in a Cretaceous forearc basin, Southern Vizcaino Peninsula, Baja California, Mexico. In: Abbot, P. L. (ed.) *Cretaceous Stratigraphy, Western North America*. Los Angeles: Pacific Section, Society of Economic Paleontologist and Mineralogists, pp. 79–90.

Busby-Spera, C. J. & White, J. D. L. (1987). Variation in peperite textures associated with differing host sediment properties. *Bulletin of Volcanology* **49**, 765–776.

Cecil, M. R., Rotberg, G. L., Ducea, M. N., Saleeby, J. B. & Gehrels, G. E. (2012). Magmatic growth and batholithic root development in the northern Sierra Nevada, California. *Geosphere* **8**, 592–606.

Chapman, J. B., Ducea, M. N., DeCelles, P. G. & Profeta, L. (2015). Tracking changes in crustal thickness during orogenic evolution with Sr/Y: an example from the North American Cordillera. *Geology* **43**, 919–922.

Clift, P., Draut, A., Kelemen, P. B., Blusztajn, J. & Greene, A. R. (2005). Stratigraphic and geochemical evolution of an oceanic arc upper crustal section: the Jurassic Talkeetna Volcanic Formation, south–central Alaska. *Geological Society of America Bulletin* **117**, 902–925.

DeBari, S. M. & Greene, A. (2011). Vertical stratification of composition, density, and inferred magmatic processes in exposed arc crustal sections. In: Brown, D. and Ryan, P. D. (eds) *Arc–Continent Collision. Frontiers in Earth Sciences*. Berlin: Springer, pp. 121–144.

DeBari, S. M. & Sleep, N. H. (1991). High-Mg, low-Al bulk composition of the Talkeetna island arc, Alaska: implications for primary magmas and the nature of arc crust. *Geological Society of America Bulletin* **103**, 37–47.

DeBari, S., Ruprecht, P. & Straub, S. (2013). Ultra-deep drilling into arc crust: Genesis of continental crust in volcanic arcs. *GeoPRISMS Newsletter* **30**. http://geoprisms.org/newsletters/workshop-report-ultra-deep-drilling-into-arc-crus-genesis-of-continental-crust-in-volcanic-arcs/

Deering, C. D., Bachmann, O., Dufek, J. & Gravley, D. M. (2011). Rift-related transition from andesite to rhyolite volcanism in the Taupo Volcanic Zone (New Zealand) controlled by crystal–melt dynamics in mush zones with variable mineral assemblages. *Journal of Petrology* **52**, 2243–2263.

D'Souza, R. J., Canil, D. & Creaser, R. A. (2015). Assimilation, differentiation, and thickening during formation of arc crust in space and time: the Jurassic Bonanza arc, Vancouver Island, Canada. *Geological Society of America Bulletin* **128**, 543–557.

Dufek, J. & Bachmann, O. (2010). Quantum magmatism: magmatic compositional gaps generated by melt–crystal dynamics. *Geology* **38**, 687–690.

Evans, B. W., Scaillet, B. & Kuehner, S. (2006). Experimental determination of coexisting iron–titanium oxides in the systems FeTiAlO, FeTiAlMgO, FeTiAlMgMnO, at 800 and 900°C, 1–4 kbar, and relatively high oxygen fugacity. *Contributions to Mineralogy and Petrology* **152**, 149–167.

Fackler-Adams, B. (1997). Volcanic and sedimentary facies, processes and tectonics of intra-arc basins: Jurassic continental arc of California and Cretaceous oceanic arc of Baja California. PhD thesis, University of California Santa Barbara, 248 pp.

Fackler-Adams, B. N. & Busby, C. (1998). Structural and stratigraphic evolution of extensional oceanic arcs. *Geology* **26**, 735–738.

Fujimaki, H., Tatsumoto, M. & Aoki, K. (1984). Partition coefficients of Hf, Zr and REE between phenocrysts and groundmasses. *Journal of Geophysical Research* **89**, B662–B672.

Gaetani, G. A., Grove, T. L. & Bryan, W. B. (1993). The influence of water on the petrogenesis of subduction-related igneous rocks. *Nature* **365**, 332–334.

Gaffney, A. M., Blichert-Toft, J., Nelson, B. K., Bizzarro, M., Rosing, M. & Albarède, F. (2007). Constraints on source-forming processes of West Greenland kimberlites inferred from Hf–Nd isotope systematics. *Geochimica et Cosmochimica Acta* **71**, 2820–2836.

Garrido, C. J., Bodinier, J.-L., Burg, J.-P., Zilinger, G., Hussain, S. S., Dawood, H., Chaudhry, M. N. & Gervilla, F. (2006). Petrogenesis of mafic garnet granulite in the lower crust of the Kohistan paleo-arc complex (Northern Pakistan): implications for intra-crustal differentiation of island arcs and generation of continental crust. *Journal of Petrology* **47**, 1873–1914.

Garrison, J. M., Reagan, M. K. & Sims, K. W. W. (2012). Dacite formation at Ilopango Caldera, El Salvador: U-series disequilibrium and implications for petrogenetic processes and magma storage time. *Geochemistry, Geophysics, Geosystems* **13**, 1–20.

Gast, P. W. (1968). Trace element fractionation and the origin of the tholeiitic and alkaline magma types. *Geochimica et Cosmochimica Acta* **32**, 1057–1086.

Gastil, R. G., Phillips, R. P. & Allison, E. C. (1975). *Reconnaissance geology of the state of Baja California*. Geological Society of America, Memoirs **140**, 170 pp.

Gelman, S. E., Deering, C. D., Bachmann, O., Huber, C. & Gutierrez, F. J. (2014). Identifying the crystal graveyards remaining after large silicic eruptions. *Earth and Planetary Science Letters* **403**, 299–306.

Gill, J. (1981). *Orogenic Andesites and Plate Tectonics*. New York: Springer.

Goldstein, S. L., O'Nions, R. K. & Hamilton, P. J. (1984). A Sm–Nd study of atmospheric dusts and particulates from

major river systems. *Earth and Planetary Science Letters* **20**, 221–236.

Gradstein, F. M., Ogg, J., Schmitz, M. D. & Ogg, G. M. (2012). *The Geologic Time Scale 2012* Amsterdam: Elsevier, pp. 1144.

Greene, A. R., DeBari, S. M., Kelemen, P. B., Blusztajn, J. & Clift, P. D. (2006). A detailed geochemical study of the island arc crust: the Talkeetna Arc section, south–central Alaska. *Journal of Petrology* **47**, 1051–1093.

Gualda, G. A. R., Ghiorso, M. S., Lemons, R. V. & Carley, T. L. (2012). Rhyolite-MELTS: a modified calibration of MELTS optimized for silica-rich, fluid-bearing magmatic systems. *Journal of Petrology* **53**, 875–890.

Haraguchi, S., Ishii, T., Kimura, J. & Ohara, Y. (2003). Formation of tonalite from basaltic magma at the Komahashi–Daini Seamount, northern Kyushu–Palau Ridge in the Philippine Sea, and growth of Izu–Ogasawara (Bonin)–Mariana arc crust. *Contributions to Mineralogy and Petrology* **145**, 151–168.

Harkins, S. A., Appold, M. S., Nelson, B. K., Brewer, A. M. & Groves, I. M. (2008). Lead isotope constraints on the origin of nonsulfide zinc and sulfide zinc–lead deposits in the Flinders Ranges, South Australia. *Economic Geology* **103**, 353–364.

Hart, S. R. (1984). A large-scale isotope anomaly in the southern hemisphere mantle. *Nature* **309**, 753–757.

Heywood, L. J. (2018). Diversity and Petrogenesis of Rhyolites from an Intra-oceanic Arc: Evidence from IODP Site U1437, Izu–Bonin Rear-arc and Surrounding Area. MS thesis, Western Washington University, Bellingham, WA.

Hochstaedter, A., Gill, J., Peters, R., Broughton, P., Holden, P. & Taylor, B. (2001). Across-arc geochemical trends in the Izu–Bonin arc: contributions from the subducting slab. *Geochemistry, Geophysics, Geosystems* **2**, 1019–1044.

Irvine, T. N. & Baragar, W. R. A. (1971). A guide to the chemical classification of the common volcanic rocks. *Canadian Journal of Earth Sciences* **8**, 523–548.

Ishizuka, O., Taylor, R. N., Milton, J. A., Nesbitt, R. W., Yuasa, M. & Sakamoto, I. (2006). Variation in the mantle sources of the northern Izu arc with time and space—Constraints from high-precision Pb isotopes. *Journal of Volcanology and Geothermal Research* **156**, 266–290.

Jagoutz, O. (2010). Construction of the granitoid crust of an island arc Part II: a quantitative petrogenetic model. *Contributions to Mineralogy and Petrology* **160**, 359–381.

Jagoutz, O. & Kelemen, P. B. (2015). Role of arc processes in the formation of continental crust. *Annual Review of Earth and Planetary Sciences* **43**, 363–404.

Jagoutz, O. & Klein, B. (2018). On the importance of crystallization–differentiation for the generation of SiO_2-rich melts and the composition build-up of arc (and continental) crust. *American Journal of Science* **318**, 29–63.

Jicha, B. R. & Brown, F. H. (2014). An age on the Korath Range and the viability of $^{40}Ar/^{39}Ar$ dating of kaersutite in Late Pleistocene volcanics, Ethiopia. *Quaternary Geochronology* **21**, 53–57.

Jicha, B. & Jagoutz, O. (2015). Magma production rates for intraoceanic arcs. *Elements* **11**, 105–112.

Johnson, D. M., Hooper, P. R. & Conrey, R. M. (1999). XRF analysis of rocks and minerals for major and trace elements on a single low dilution Li-tetraborate fused bead. *Advances in X-Ray Analysis* **41**, 843–867.

Knaack, C., Cornelius, S. B. & Hooper, P. R. (1994). *Trace Element Analyses of Rocks and Minerals by ICP-MS*. Pullman, WA: Washington State University GeoAnalytical Lab.

Kodaira, S., Sato, T., Takahashi, N., Miura, S., Tamura, Y., Tatsumi, Y. & Kaneda, Y. (2007). New seismological constraints on growth of continental crust in the Izu–Bonin intra-oceanic arc. *Geology* **35**, 1031–1034.

Kuiper, K. F., Deino, A., Hilgen, F. J., Krijgsman, W., Renne, P. R. & Wijbrans, J. R. (2008). Synchronizing rocks clocks of Earth history. *Science* **320**, 500–504.

Lechler, P. J. & Desilets, M. O. (1987). A review of the use of loss on ignition as a measurement of total volatiles in whole-rock analysis. *Chemical Geology* **63**, 341–344.

Lee, C. A. & Bachmann, O. (2014). How important is the role of crystal fractionation in making intermediate magmas? Insights from Zr and P systematics. *Earth and Planetary Science Letters* **393**, 266–274.

Le Maitre, R.W. (1989). *A Classification of Igneous Rocks and Glossary of Terms.* Cambridge: Cambridge University Press.

Lemarchand, F., Villemant, B. & Calas, G. (1987). Trace element distribution coefficients in alkaline series. *Geochimica et Cosmochimica Acta* **51**, 1071–1081.

Lieu, W. K. & Stern, R. J. (2019). The robustness of Sr/Y and La/Yb as proxies for crust thickness in modern arcs. *Geosphere* **15**, 1–21.

Lipman, P. & Bachmann, O. (2015). Ignimbrites to batholiths: Integrating perspectives from geological, geophysical, and geochronological data. *Geosphere* **11**, 705–743.

Lundstrom, C. C. & Glazner, A. F. (2016). Silicic magmatism and the volcanic–plutonic connection. *Elements* **12**, 91–96.

Mantle, G. W. & Collins, W. J. (2008). Quantifying crustal thickness variations in evolving orogens: correlation between arc basalt composition and Moho depth. *Geology* **36**, 87–90.

Medynski, S. M., Busby, C., DeBari, S. M., Morris, R. A., Andrews, G. D., Brown, S. R. & Schmitt, A. (2016). The upper- to middle-crustal section of the Alisitos oceanic arc, (Baja Mexico): and analog of the Izu-Bonin-Marianas (IBM) arc. *American Geophysical Union, Abstracts*. Paper No. V13C-2866.

Min, K., Mundil, R., Renne, P. R. & Ludwig, K. R. (2000). A test for systematic errors in $^{40}Ar/^{39}Ar$ geochronology through comparison with U/Pb analysis of a 1·1-Ga rhyolite. *Geochimica et Cosmochimica Acta* **64**, 73–98.

Morgan, J., Arrowsmith, R., Atekwana, E., Behn, M., Benoit, M., Bilek, S., Deshon, H., Ellis, S., Evans, R., Flemings, P., Freymueller, J., Gomberg, J., Gurnis, M., Jaeger, J., Haeussler, P., Levin, V., Kelley, K., Kelsey, H., Kent, A., Keranen, K., Litchfield, N., Lizarralde, D., Marsaglia, K., Oskin, M., Pazzaglia, F., Pritchard, M., Roering, J., Rooney, T., Saffer, D., Schwartz, S., Shillington, D., Thurber, C., Trehu, A., Underwood, M., van Averndonk, H., van Wijk, J., Wallace, L., Wang, K., Withjack, M., Wysoczanski, R. & Yogodzinski, G. (2013). National Science Foundation GeoPRISMS Implementation Plan 2, Subduction Cycles and Deformation. MARGINS. http://geoprisms.org/research/science-plan/

Nandedkar, R. H., Ulmer, P. & Müntener, O. (2014). Fractional crystallization of primitive, hydrous arc magmas: an experimental study at 0·7 GPa. *Contributions to Mineralogy and Petrology* **167**, 1–27.

Nandedkar, R. H., Hürlimann, N., Ulmer, P. & Müntener, O. (2016). Amphibole–melt trace element partitioning of fractionating calc-alkaline magmas in the lower crust: an experimental study. *Contributions to Mineralogy and Petrology* **171**, 1–25.

Paster, T. P., Schauwecker, D. S. & Haskin, L. A. (1974). The behavior of some trace elements during solidification of the Skaergaard layered series. *Geochimica et Cosmochimica Acta* **38**, 1549–1577.

Paton, C., Woodhead, J. D., Hellstrom, J. C., Hergt, J. M., Greig, A. & Maas, R. (2010). Improved laser ablation U–Pb zircon geochronology through robust downhole fractionation correction. *Geochemistry, Geophysics, Geosystems* **11**, 1–36.

Pearce, J. A. & Peate, D. W. (1995). Tectonic implications of the composition of volcanic arc magmas. *Annual Review of Earth and Planetary Sciences* **23**, 251–286.

Petrus, J. A. & Kamber, B. S. (2012). VizualAge: a novel approach to laser ablation ICP-MS U–Pb geochronology data reduction. *Geostandards and Geoanalytical Research* **36**, 247–270.

Peucat, J. J., Vidal, P., Bernard-Griffiths, J. & Condie, K. C. (1988). Sr, Nd, and Pb isotopic systematics in the Archaean low- to high-grade transition zone of southern India: syn-accretion vs. post-accretion granulites. *Journal of Geology* **97**, 537–550.

Plank, T., Kelley, K. A., Zimmer, M. M., Hauri, E. H. & Wallace, P. J. (2013). Why do mafic arc magmas contain ~4 wt% water on average. *Earth and Planetary Science Letters* **364**, 168–179.

Rudnick, R. L. (1995). Making continental crust. *Nature* **378**, 571–578.

Sha, L. K. & Chappell, B. W. (1999). Apatite chemical composition, determined by electron microprobe and laser-ablation inductively coupled plasma mass spectrometry, as a probe into granite petrogenesis. *Geochimica et Cosmochimica Acta* **63**, 3861–3881.

Sisson, T. W. & Grove, T. L. (1993). Experimental investigations of the role of H_2O in calc-alkaline differentiation and subduction zone magmatism. *Contributions to Mineralogy and Petrology* **113**, 143–166.

Squires, R. L. (2018). Late Cretaceous endemic shallow-marine gastropod genera of the northeast Pacific: biodiversity and faunal changes. *PaleoBios* **35**, 1–16.

Steenberg, L., Boroughs, S. & Knaack, C. (2017). Estimation of accuracy and precision for trace elements analyzed by inductively coupled plasma mass spectrometry (ICP-MS) at the Peter Hooper Geoanalytical Laboratory, Washington State University. *Geological Society of America, Abstracts with Programs* **49**. Paper No. 69-3.

Stern, R. J., Fouch, M. J. & Klemperer, S. L. (2003). An overview of the Izu–Bonin–Mariana subduction factory. *Geophysical Monograph Series* **138**, 175–222.

Straub, S. (2008). Uniform processes of melt differentiation in the central Izu–Bonin volcanic arc (NW Pacific). In: Annen, C. and Zellmer, G. F. (eds) *Dynamics of Crustal Magma Transfer, Storage and Differentiation. Geological Society*, London, Special Publications **304**, 261–283.

Sun, S. S. & McDonough, W. F. (1989). Chemical and isotopic systematics of oceanic basalts; implications for mantle composition and processes; magmatism in the ocean basins. In: Saunders, A. D. and Norry, M. J. (eds) *Magmatism in the Ocean Basins. Geological Society*, London, Special Publications **42**, 313–345.

Sun, C. H. & Stern, R. J. (2001). Genesis of Mariana shoshonites: contribution of the subduction component. *Journal of Geophysical Research: Solid Earth* **106**, 589–608.

Suyehiro, K., Takahashi, N., Ariie, Y., Yokoi, Y., Hino, R., Shinohara, M., Kanazawa, T., Hirata, N., Tokuyama, H. & Taira, A. (1996). Continental crust, crustal underplating, and low-Q upper mantle beneath an oceanic island arc. *Science* **272**, 390–392.

Takahashi, N., Kodaira, S., Klemperer, S. L., Tatsumi, Y., Kaneda, Y. & Suyehiro, K. (2007). Crustal structure and evolution of the Mariana intra-oceanic island arc. *Geology* **35**, 203–206.

Tatsumi, Y. & Stern, R. (2006). Manufacturing continental crust in the subduction factory. *Oceanography* **19**, 104–112.

Tiepolo, M., Oberti, R. & Zanetti, A. (2007). Trace-element partitioning between amphibole and silicate melt. In: Hawthorne, F. C., Oberti, R., Della Ventura, G. and Mottana, A. (eds) *Amphiboles: Crystal Chemistry, Occurrence, and Health Issues. Mineralogical Society of America and Geochemical Society, Reviews in Mineralogy and Geochemistry* **67**, 417–452.

Tollstrup, D., Gill, J., Kent, A., Prinkey, D., Williams, R., Tamura, Y. & Ishizuka, O. (2010). Across-arc geochemical trends in the Izu–Bonin arc: contributions from the subducting slab, revisited. *Geochemistry, Geophysics, Geosystems* **11**, 1–27.

Wallace, P. J. (2005). Volatiles in subduction zone magmas: concentrations and fluxes based on melt inclusion and volcanic glass data. *Journal of Volcanogy and Geothermal Research* **140**, 217–240.

Waters, L. E. & Lange, R. A. (2015). An updated calibration of the plagioclase–liquid hygrometer–thermometer applicable to basalts through rhyolites. *American Mineralogist* **100**, 2172–2184.

White, J. D. L. & Busby-Spera, C. J. (1987). Deep marine arc apron deposits and syndepositional magmatism in the Alisitos Group at Punta Cono, Baja California, Mexico. *Sedimentology* **34**, 911–927.